

©2015

Matthew Yunching Lu

ALL RIGHTS RESERVED

INVESTIGATION OF PHYSICAL AND ELECTROCHEMICAL PROPERTIES OF
TANTALUM-DOPED BETA NIOBIUM PHOSPHATE AS AN ELECTRODE FOR
LITHIUM BATTERIES

By

MATTHEW YUNCHING LU

A thesis submitted to the

Graduate School-New Brunswick

Rutgers, The State University of New Jersey

In partial fulfillment of the requirements

For the degree of

Master of Science

Graduate Program in Materials Science and Engineering

Written under the direction of

Glenn G. Amatucci

And approved by

New Brunswick, New Jersey

October 2015

ABSTRACT OF THE THESIS

Investigation of Physical and Electrochemical Properties of Tantalum-Doped Beta Niobium Phosphate as an Electrode for Lithium Batteries

By MATTHEW YUNCHING LU

Thesis Director:

Glenn G. Amatucci

Phosphate intercalation materials are an integral chemistry for secondary lithium-ion batteries. The demand for energy storage technologies with higher energy and power densities is ever increasing, indicating a necessity for the development of new battery chemistries. The robust nature of phosphate groups is a strong platform for the development of new lithium-ion battery chemistries. From here, β -NbPO₅ is realized as a positive electrode material for lithium batteries. With an operating voltage circa 2V, β -NbPO₅ has the potential to be either the positive or negative electrode. In this thesis, the electrochemical stability of β -NbPO₅ is improved using two different methods of altering the voltage window and utilizing a Ta⁵⁺ ionic substitution to form β -Ta_xNb_{1-x}PO₅. Preliminary electrochemistry of the end member β -TaPO₅ is reported for the first time. The flat voltage profile, excellent reversibility, and low polarization make β -Ta_xNb_{1-x}PO₅ a good candidate for a model reference electrode material.

Acknowledgment

Dr. Glenn Amatucci has provided endless guidance in my academics, research, and future career. As an undergraduate and graduate student in the Energy Storage Research Group for the past three years, I am extremely grateful for his infinite patience and wisdom. He has provided the funding and encouragement to complete my James J. Slade Scholar Project, Senior Project, and Master's Thesis in my four years at Rutgers University. My pursuit to continue to my career by beginning my journey for a degree of Doctor of Philosophy this coming Fall would not have been possible without Dr. Amatucci.

I would also like to show my appreciation to my committee members Dr. Lisa Klein and Dr. Frederic Cosandey. Dr. Klein has played an instrumental role in both my undergraduate and graduate career. My graduate career would not have been made possible without all of the assistance and effort put forth by Dr. Klein, who went above and beyond to ensure the completion of my Master's Degree. Both Dr. Klein and Dr. Cosandey are excellent professors that have guided me and many other students through the quandaries of Materials Science.

An additional thank you to Dr. Nathalie Pereira for training me as an undergraduate to enable me to complete my research at the graduate level. Because of my training and all the members of ESRG, I am confident in continuing my career as both a researcher and engineer. I am incredibly thankful for their assistance in my projects and daily discussions that created such an enjoyable work environment. Thank you to staff members Dr. Kimberly Scott, Mrs. Fadwa Badway, Mrs. Linda Sung, Mrs. Irene Plitz, Mrs. Anna Halajko, Mr. Barry Vanning, and Mr. John Gural, past graduate students Dr.

Jonathan Ko and Dr. Anthony Ferrer, current graduate students Mr. Joshua Kim and Mr. Nicholas Faenza, past undergraduate students Greg and Sheel; and the current undergraduate George—best of luck in taking over my position.

A special thank you to my roommates and essentially brothers Alvin, Joe, and Marvin for their ceaseless entertainment and academic, social, and emotional support over the past four years. Thank you to Moiz, David, Brian, Desmond, and Terri for always being there to encourage me to dream big and live life to the fullest. Thank you to past members of the Scarlet Aquatic Club swim team Kendrick, Chris, Rich, Carl, and my coach Dave, for instilling an unimaginable work ethic that has carried over to every aspect of my life. You guys have proven to me that no matter how hard things get, at least I am not at swim practice.

Thank you to my sisters and role models Rachel and Lisa for constantly providing a path for me to travel that is filled with expectations of living up to the legacy of the Lu children. This pursuit to be just as successful motivates me to be the best engineer, swimmer, runner, and brother that I can be. Thank you to my dog Lucky for always having the brightest smile even on the darkest of days. It is always heartening to know that there is a warm and welcoming family to come home to that will provide me with unconditional love.

The financial support of the US Government is acknowledged.

The work in Chapter 3 has yet to be submitted for publication as of September 2015. The work was completed with F. Badway, J. R. Kim, and G. G. Amatuucci.

Dedication

I dedicate this thesis to my parents Su-Jen and Mark for always believing in their children and allowing us to pursue our own passions. I am forever thankful for having parents who prioritize their children above all else and provide us with the emotional and financial support in any and every situation. My upbringing has undoubtedly pushed me to become who I am today. I hope to one day become at least half the engineer of my father and to one day provide the compassion and hospitality my mother has given to our family. Words can never express how important my parents are to me, and none of this would have been possible without my entire family. Although it can never be said enough, I love you all.

Table of Contents

ABSTRACT OF THE THESIS	ii
Acknowledgment	iii
Dedication	v
Table of Contents	vi
List of Tables	viii
List of Figures	ix
1 Introduction.....	1
1.1 Energy Storage and Batteries	1
1.2 Lithium-ion Battery Technology	3
1.3 Negative Electrodes	5
1.4 Electrolytes	7
1.5 Positive Electrodes	9
1.6 Coin Cell Batteries.....	10
1.7 Phosphates	11
1.8 Beta Niobium Phosphate	12
1.9 Alpha and Orthorhombic Niobium Phosphate	16
1.10 Ionic Substitutions.....	18
1.11 Research Plan	19
2 Experimental	20
2.1 Synthesis.....	20
2.2 X-ray Diffraction	23

2.3	Rietveld Refinement	28
2.4	Galvanostatic Cycling and Rate Protocols for Half Cells	29
2.5	Potentiostatic Intermittent Titration Technique.....	30
3	Investigation of Physical and Electrochemical Properties of β -Ta _x Nb _{1-x} PO ₅ as an Electrode for Lithium Batteries	32
3.1	Results	32
3.1.1	Structure	32
3.1.2	Electrochemistry.....	37
3.2	Discussion.....	45
3.2.1	Electrochemistry.....	45
3.2.2	Phase Evolution.....	48
4	Future Work	55
5	Summary	57
6	References	58

List of Tables

Table 1-1 Ionic radii with coordination VI of selected ions. ²⁹	18
Table 2-1 Annealing conditions.....	20
Table 3-1 Composition of 4g batches containing varying amounts of excess phosphorus.	34
Table 3-2 Purity of 0% and 2% Ta samples quenched from different temperatures.	34
Table 3-3 Rietveld refinement data for various molar % Ta substitutions for Nb in NbPO ₅ . All samples were quenched from 1350°C.	36
Table 3-4 Discharge capacities of the first cycle at 7.5 mA·g ⁻¹ from 2.8 V to 1.75 V.	37
Table 3-5 Rietveld analysis of patterns <i>ex-situ</i> cells.....	49
Table 3-6 Rietveld analysis of <i>ex-situ</i> XRD of the unsubstituted samples.....	53
Table 3-7 Rietveld analysis of <i>ex-situ</i> XRD of 10% Ta samples.	54

List of Figures

Figure 1-1 Galvanic cell (a) and electrolytic cell (b) schematic.	2
Figure 1-2 Intercalation (top) and conversion (bottom) reactions in lithium batteries.	4
Figure 1-3 Components of a coin cell battery.....	10
Figure 1-4 β -NbPO ₅ unit cell viewed from the [010] direction with NbO ₆ octahedra (green) and PO ₄ tetrahedra (blue).	13
Figure 1-5 Monoclinic (black) supercell and orthorhombic (green) subcells.....	13
Figure 1-6 Nb ₂ O ₅ -P ₂ O ₅ phase diagram redrawn in part from Levin and Roth. ¹⁴	15
Figure 1-7 Structure of tetragonal α -NbPO ₅ from the [001] direction.	16
Figure 1-8 Orthorhombic unit cell shown from the [010] direction.	17
Figure 2-1 X-ray spectrum of characteristic and braking radiation with a Cu target and Ni filter.....	24
Figure 2-2 Illustration of Bragg's Law.	25
Figure 2-3 Current response to a small negative (left) and positive (right) potential step change.	30
Figure 3-1 XRD patterns for NbPO ₅ synthesized using solid state methods with quenching from 300°C (a) and 1350°C (b), and solution methods with quenching from 300°C (c) and 1350° (d). Circles indicate the tetragonal α -NbPO ₅ phase and stars indicate the monoclinic β -NbPO ₅ phase.....	33
Figure 3-2 XRD patterns for various percentages of Ta ⁵⁺ substitution in Ta _x Nb _{1-x} PO ₅ quenched at 1350°C: (a) 0%, (b) 2%, (c) 5%, (d) 10%, (e) 20%, and (f) 100% Ta. Miller indices are given for the monoclinic Beta phase.	36

Figure 3-3 1 st and 75 th discharge profiles for (a) 0%, (b) 2%, (c) 5%, (d) 10%, and (e) 20% Ta substitutions at 7.5 mA·g ⁻¹ from 2.8V to 1.75V.....	38
Figure 3-4 Percent capacity retention for Ta substitutions at 22.5 mA·g ⁻¹ (a). Capacity drop from cycles 13 to 21 are due to the increase in current from rate testing. Percent capacity retention for Ta substitutions at high currents (b) all cycled from 2.8V to 1.75V.....	39
Figure 3-5 First cycle for 0% Ta samples cycled down to different cutoff voltages with a 7.58 mA·g ⁻¹ current (a) with discharge capacity retention during extended cycling (b).....	40
Figure 3-6 1 st and 85 th cycle voltage profiles for different cutoff voltages: (a) 1.85 V, (b) 1.75 V, (c) 1.625 V, (d) 1.5 V, and (e) 1.25 V.....	41
Figure 3-7 0-10% Ta substitutions cycled from 2.8V-1.75V and an unsubstituted sample cycled from 2.8V-1.85V.	42
Figure 3-8 Voltage profiles for TaPO ₅ from 3V to 1V (a) and 3V to 0.75V (b) both at 7.58 mA·g ⁻¹ , and 2.5V to 0.075V at 10 mA·g ⁻¹ (c).	44
Figure 3-9 PITT results for 0% (a), 2% (b), 5% (c), 10% (d), and 20% (e) Ta to different cutoff voltages with a 10mV step and 2mA·g ⁻¹ current cutoff.	46
Figure 3-10 PITT results for 5% Mo (a) and 10% Mo (b) to different cutoff voltages with a 10mV step and 2mA·g ⁻¹ current cutoff.	47
Figure 3-11 Rietveld analysis of 0% Ta at 1.90V (a) and 1.75V (b) and 10% Ta at 1.90V (c) and 1.75V (d). Black lines are experimental data, red lines are theoretical, and gray lines are difference calculations.....	50

Figure 3-12 <i>Ex-situ</i> XRD patterns of unsubstituted samples during delithiation (a)	
corresponding with their respective positions in the voltage profile (b).	53
Figure 3-13 <i>Ex-situ</i> XRD patterns of 10% Ta samples during delithiation (a)	
corresponding with their respective positions in the voltage profile (b).	54

1 Introduction

1.1 Energy Storage and Batteries

Energy storage has bottlenecked many technical industries in the past few years, resulting in a strong demand for improved energy storage solutions. One of the most common forms of energy storage is electrochemical storage usually in the form of a battery. Batteries store and deliver electrochemical energy through oxidation-reduction reactions between two electrodes immersed in an electrolyte. The electrolyte provides a medium for ionic transportation inside the cell while electrons flow through an external circuit to balance the charge transfer, thus generating a current. When a cell is discharging, the negative electrode is the anode where an oxidation reaction occurs to separate ions and electrons and the positive electrode is the cathode where a reduction reaction occurs. Depending on the thermodynamics of the electrodes, different battery chemistries will provide different specific energy and power densities. Because of this, batteries can be found in a multitude of applications such as in vehicles, power grid storage, and various electronic devices. However, the development of batteries is often referred to as sluggish and the weakest link in portable electronics.

A prime example of this slow development is the lead-acid chemistry used in automobiles. In the twenty-first century, cars still employ the same lead-acid chemistry developed in 1860 by Raymond Louis Gaston Planté.¹ Over the years, many chemistries have been developed, but no single chemistry has triumphed as the optimal battery. The perfect battery would have high power, high capacity, low weight, low cost, high safety, and ease in manufacturing, but trade-offs make it effectively impossible to develop a battery to satisfy all of these categories. The sluggish progress of battery technology has

resulted in many researchers around the world tackling this problem to find a seemingly impossible solution.

The most ubiquitous battery in portable electronics utilizes a similar theme based on the LiCoO_2 and carbon graphite “Li-ion” cell concept that Sony first commercialized in 1991.² In a Li-ion battery, there is a positive electrode and negative electrode immersed in an electrolyte as pictured in Fig. 1-1. During discharge, the battery a galvanic cell with the positive terminal being the cathode that receives the electron flow which is the opposite direction of the current flow by convention. The lithium ions travel through the electrolyte and separator from the anode and into the cathode. To balance out charges, an electron flows through an external circuit from the anode to the cathode thus providing a current. During charge, the battery is an electrolytic cell and the positive electrode becomes the anode and then negative electrode becomes the cathode.

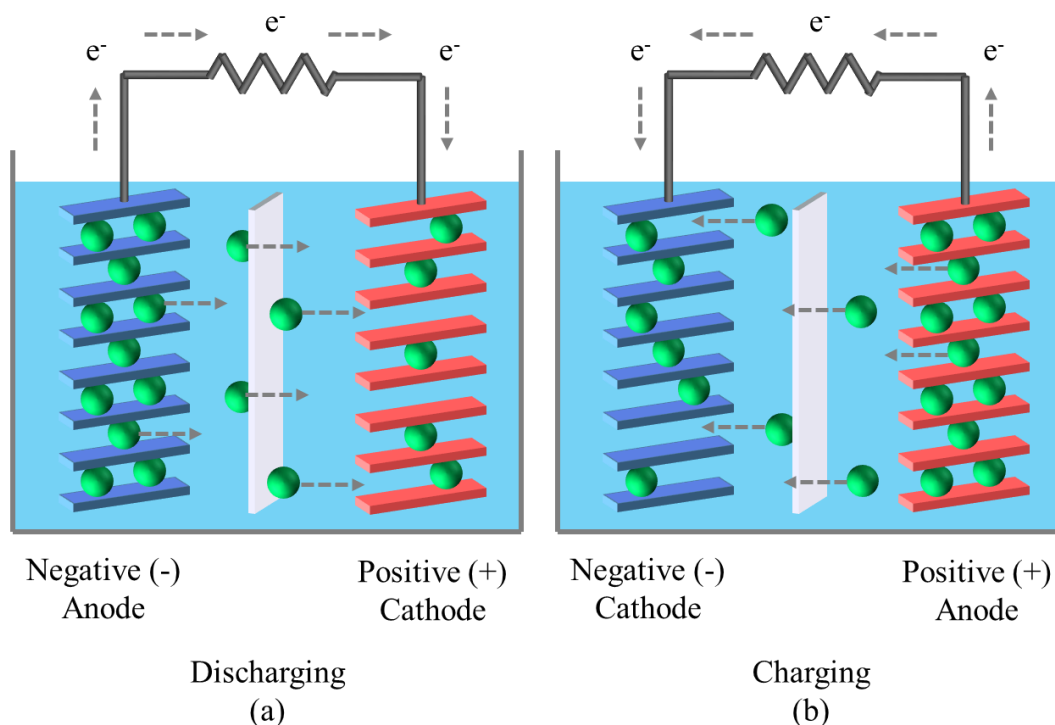
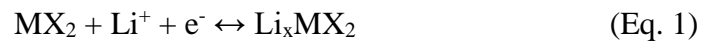


Figure 1-1 Galvanic cell (a) and electrolytic cell (b) schematic.

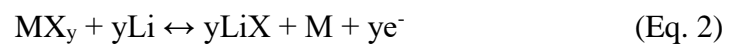
1.2 Lithium-ion Battery Technology

Lithium-ion batteries are incredibly widespread for good reason. Located in the top left corner of the periodic table, lithium is one of the smallest and lightest elements. This is optimal for the consumer market since lighter batteries increase portability and smaller atoms typically allow for higher diffusion rates for faster charging and discharging. There are two types of lithium-ion batteries, primary and secondary. Primary batteries can only be discharged once, whereas a secondary battery is rechargeable. Both batteries have the same configuration of electrodes and separators, but secondary cells are dependent on the battery chemistry having a reversible reaction. Lithium-ions can be transferred between the positive and negative electrode in two methods, intercalation and conversion reactions. An intercalation reaction is depicted in the top of Fig. 1-2 where lithium atoms are inserted between the layers or channels in the crystal structure. This is seen in materials such as LiCoO_2 , LiFePO_4 , LiMnO_2 , and graphite. An intercalation reaction can follow the reaction:



In conversion materials, the entire structure changes as the electrode reacts with lithium, shown in the bottom of Fig. 1-2. This can allow for more than one lithium atom per transition metal atom due to multiple valence states, allowing for higher theoretical capacities. However, some conversion electrodes suffer from poor reversibility and rate capabilities and therefore methods to improve their performance are being studied.^{3,4}

Conversion reactions containing halides generally follow the form:



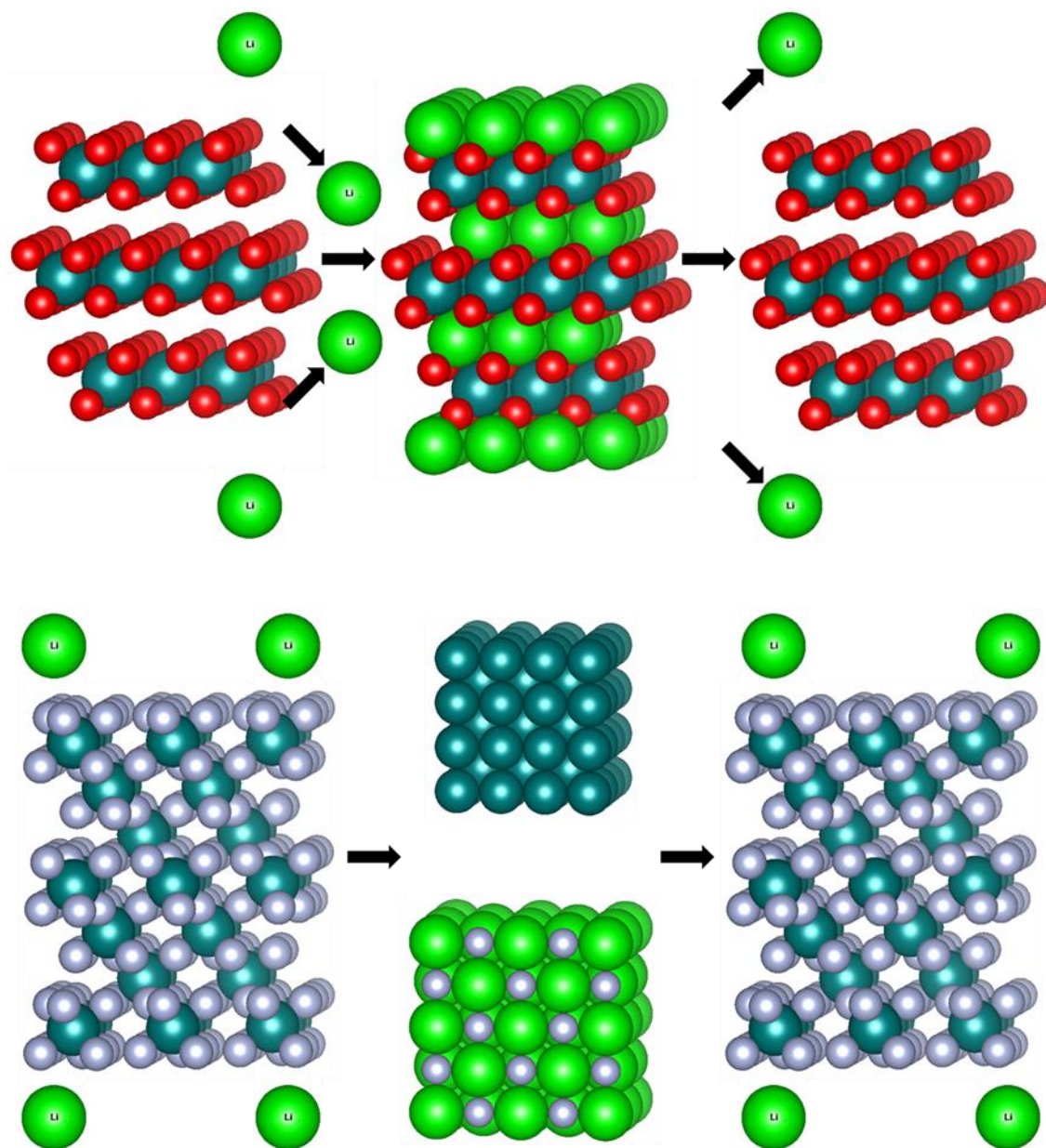


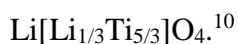
Figure 1-2 Intercalation (top) and conversion (bottom) reactions in lithium batteries.

1.3 Negative Electrodes

Also known as the anode during discharge, the negative electrode is typically graphite or lithium metal. Lithium metal is an optimal candidate for the negative electrode because it is the lightest solid element at $6.94\text{g}\cdot\text{mol}^{-1}$, the most electropositive metal at -3.04V against a standard hydrogen electrode, and the least dense at $0.53\text{g}\cdot\text{cm}^{-3}$.⁵ However, this alkali metal poses issues because of its high reactivity. On contact with air, lithium reacts exothermically with oxygen and water. Lithium batteries have been targeted in the media as explosive and dangerous, being the culprit of battery fires in airplanes, electric buses, taxis, cellphones, and laptops.⁶ Furthermore, repeated charging is known to form mossy and dendritic structures that can pierce through the separator and create a short circuit with the positive electrode. Any non-uniformity in the electrode, including the random orientation of the particles, can cause a non-uniform charge distribution and uneven lithium plating. These regions have an increased surface area and repeated cycling will promote the growth of these deleterious structures. Because of such, lithiated carbon is a commonly used negative electrode with its relative safety and similar chemical potential to lithium metal. Graphitic carbon accepts one lithium atom per six carbon atoms (LiC_6) that sits in between the graphene sheets as seen in the intercalation model in Fig. 1-2, giving a theoretical specific capacity of $372\text{mAh}\cdot\text{g}^{-1}$.

Other negative electrode materials have been researched and shown to have exceptional theoretical specific capacities, such as Si ($4200\text{mAh}\cdot\text{g}^{-1}$), Mg ($2205\text{mAh}\cdot\text{g}^{-1}$), Na ($1166\text{mAh}\cdot\text{g}^{-1}$), Zn ($820\text{mAh}\cdot\text{g}^{-1}$), and $\text{Li}_{3-x}\text{Co}_x\text{N}$ ($600\text{mAh}\cdot\text{g}^{-1}$).⁷⁻⁹ However, all the above except for the latter suffer from more than 300% volumetric expansion of the resulting lithium based alloys, causing internal stresses that can lead to performance

losses and battery failure. Thus, it is common to see lithiated carbon and other materials that show little to no volumetric expansion over repeated cycling, such as



Typical lithium batteries employ a rocking chair method where the lithium is “rocked” between the positive and negative electrodes during charge and discharge. When a battery is first cycled, a passivation layer or solid electrolyte interface (SEI), forms on the surface of the negative electrode that contacts the electrolyte. This thin and highly resistive layer prevents the cell from self-discharging during storage, giving lithium batteries long shelf lives. The thin layer does not adversely affect the performance of the cell, unless the layer grows too thick. Long storage times and heated conditions may cause the layer to grow. It is possible to prevent the growth of the passivation layer by maintaining a light load or sporadically running a high load during storage.

1.4 Electrolytes

The electrolyte serves as a medium for ionic transportation between the positive and negative electrodes. It is imperative that the electrolyte has high enough ionic conductivity to enable ionic transport at sufficient rates, while being electrically insulating as to prevent a short circuit of the battery. Of course, the electrolyte must be chemically stable with the electrodes and must be able to quickly form a passivation layer with the negative electrode. Electrolytes are highly reactive and it is preferable to be made from safe materials that are nonflammable and nonexplosive in the event of a short circuit. Large electrochemical windows are also preferred, since there is a large demand for high power batteries that require stable electrolytes at high voltages.

There are several types of electrolytes, primarily solid and liquid. It is critical that an electrolyte remains in the same state of matter over the entire working temperature range. The scope of this thesis will only cover liquid electrolytes, of which there are organic and ionic electrolytes.

Organic liquid electrolytes such as carbonates, esters, and ethers are good solvents for lithium salts and are currently used in commercial technology. Typical oxidation potentials (highest occupied molecular orbital, HOMO) are around 4.7V and reduction potentials (lowest unoccupied molecular orbitals, LUMO) are around 1.0V against Li/Li⁺. A wide potential window is desired for the HOMO and LUMO levels to ensure stability of the electrolyte during operation. The viscosity of electrolytes is also an important factor that impacts the activation energy required for ionic diffusion. Electrolytes containing carbonates generally have low viscosities, allowing for high rates of diffusion. Thus, the most common organic liquid electrolytes contain carbonates or carbonate

blends such as diethyl carbonate (DEC), dimethyl carbonate (DMC), ethylene carbonate (EC), ethylmethyl carbonate (EMC), and propylene carbonate (PC). This thesis utilizes LiPF_6 dissolved in a 1:1 mixture of EC:DMC. EC is good at dissolving lithium salts because of its high dielectric constant, but it also has a high viscosity. Thus it is mixed with DMC, which has a low viscosity and low melting temperature. This results in an electrolyte with the best properties from EC and DMC.

On the other hand, ionic liquid electrolytes contain lithium salts that are molten at room temperature. The advantage of ionic liquids is that they have low vapor pressures and large voltage windows for electrochemical stability with some electrolytes achieving up to 6V.¹¹ As research progresses, the development of ionic liquid electrolytes can allow for new electrode materials that operate at high voltages enabling higher power batteries.

Of the electrolytes mentioned, all are nonaqueous as small contents of water can react with different components of a lithium battery causing drops in performance or complete failure. The most commonly used LiPF_6 based electrolyte forms the vitriolic HF in the presence of water. Lithium is also highly reactive with water, forming LiOH , hydrogen, and heat.

1.5 Positive Electrodes

Also known as the cathode on discharge, positive electrodes garner more research focus than negative electrodes because of the great potential remaining to improve battery technology. Positive electrodes are similar to negative electrodes in their reaction mechanisms with lithium shown back in Fig. 1-2. Intercalation materials accept one lithium per transition metal atom, whereas conversion materials can access multiple valence states of each transition metal atom giving high theoretical specific capacities. The first reversible insertion electrode was developed by Whittingham in 1976 with LiTiS_2 . There are several different types of positive electrodes, the most popular being layered oxides (LiCoO_2 , LiMnO_2 , LiNiCoAlO_2), spinels (LiMn_2O_4), and phosphates (LiFePO_4). Each type of battery displays their own strengths in various categories such as cost, safety, reliability, specific energy, and specific power, but no single battery excels in all categories. As always, there are tradeoffs between maximizing performance in one category at the cost of another, thus making battery selection dependent on the requirements of the application. The focus of this thesis is on phosphate batteries that provide good rate capabilities and safety, but lack energy density in comparison to other Li-ion technologies.

1.6 Coin Cell Batteries

The standard battery is composed of a sandwich of layers, all playing critical roles in the function of the battery. Fig. 1-3 shows a typical setup for a small aluminum coin cell battery used in this thesis, which is usually filled with a liquid electrolyte that is not pictured. There is the base casing, positive electrode, gasket, separator, negative electrode, spacer, spring, and top casing. The casing pieces act as current collectors and terminals for electronic connection to an external circuit. The positive and negative electrodes are the main topics of research studies and define the battery type. The gasket is used to create a semi-hermetic seal and also prevent contact between the top and base casing when the cell is clamped shut. The separator provides an electronic barrier to prevent a short circuit while simultaneously allowing ions to flow across. The spacer and spring ensure contact between all the pieces of the cell.

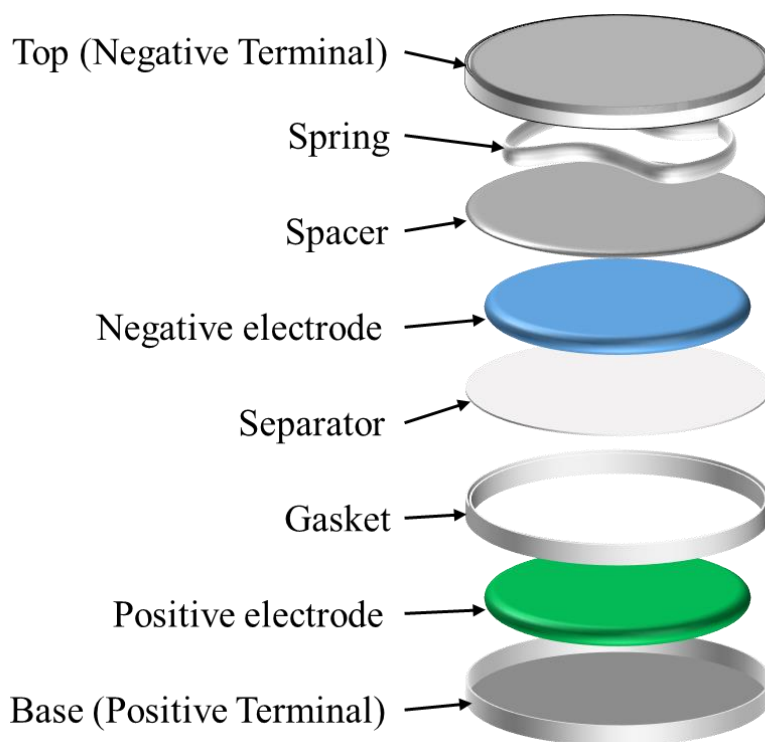


Figure 1-3 Components of a coin cell battery.

1.7 Phosphates

Phosphates as positive electrodes were first introduced with the triphylite LiFePO_4 by Padhi et al. in 1997.¹² This phospholivine is a low cost and environmentally friendly option that uses the earth abundant Fe as opposed to the toxic Co seen in LiCoO_2 batteries introduced by Sony in 1991.² Batteries containing phosphates have the intrinsic advantage of robust covalent bonding between P and O. Each P atom is tetrahedrally coordinated to O, creating an open network for facile diffusion and lithium insertion. Because of this tough and open bonding structure, phosphate batteries can cycle at high rates. Furthermore, stronger bonds result in more resistance to overcharging and thermal degradation, creating safer batteries. The downfall, however, is that PO_4 groups are heavy and voluminous in comparison to oxide groups that only have a few O atoms per transition metal atom, thus decreasing the specific energy of phosphate materials. Because there are two anions per transition metal, this class of materials benefits from the polyanion inductive effect. The O atoms are permanently polarized towards the more electronegative PO_4 tetrahedra, thus lowering the covalent character of the M-O bond. This results in an increased potential of the $\text{M}^{5+}/\text{M}^{4+}$ redox couple that is responsible for lithium insertion. The topic of this study is on niobium phosphates, specifically $\beta\text{-NbPO}_5$, an intercalation material that seems to exhibit excellent electrochemical reversibility but has not been widely studied.

1.8 Beta Niobium Phosphate

Niobium phosphate, NbPO_5 , was first synthesized and reported by Hahn in 1951.¹³ The high temperature β - NbPO_5 phase was reported by Levin and Roth,¹⁴ and later refined by Chahboun.¹⁵ LeClaire¹⁶ confirmed a monoclinic supercell and orthorhombic subcell with a single crystal study that is used as the reference in this study. The monoclinic unit cell of space group $P2_1/c$ ($Z = 8$) has parameters: $a = 13.0969(16) \text{ \AA}$, $b = 5.2799(6) \text{ \AA}$, $c = 13.2281(16) \text{ \AA}$, $\beta = 120.334(8)^\circ$, $V = 789.49755 \text{ \AA}^3$, and is illustrated in Fig. 1-4 from the [010] direction. The simplified orthorhombic cell relates to the monoclinic cell: $a_o = a_m \sin \beta$, $b_o = b_m$, $c_o = c_m/2$ and is illustrated in Fig. 1-5 to clarify the relationship between the monoclinic (black) supercell and orthorhombic (green) subcell. NbPO_5 is the second member ($m = 2$) of the monophosphate tungsten bronze series with pentagonal tunnels that follows the formula $\text{A}_x(\text{WO}_3)_{2m}(\text{PO}_2)_4$ ($A = \text{Ag, Li, Na}$). The pentagonal tunnels align with the [010] axis and allow for insertion of small atoms, allowing for electrochemical energy storage. The remainder of the crystal structure is composed of ribbons of NbO_6 octahedra separated by PO_4 tetrahedra in ReO_3 type chains. NbPO_5 is isostructural with other materials such as TaPO_5 ,¹⁵ TaVO_5 ,¹⁷ TiSO_5 ,¹⁸⁻²⁰ ϵ - VPO_5 ,^{21,22} and WPO_5 .^{23,24} The majority of these phases all possess electrochemical intercalation properties because of the pentagonal tunnels.

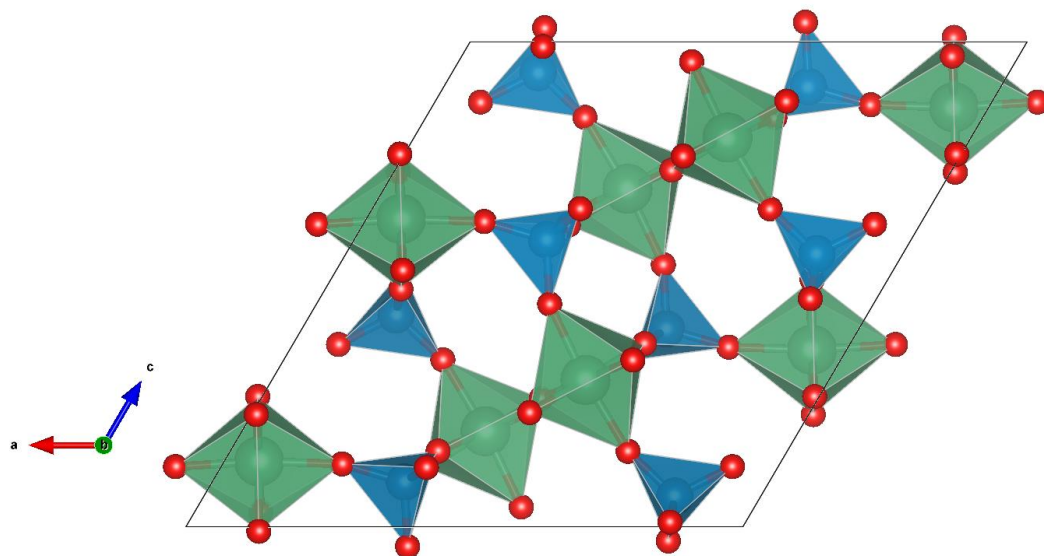


Figure 1-4 β -NbPO₅ unit cell viewed from the [010] direction with NbO₆ octahedra (green) and PO₄ tetrahedra (blue).

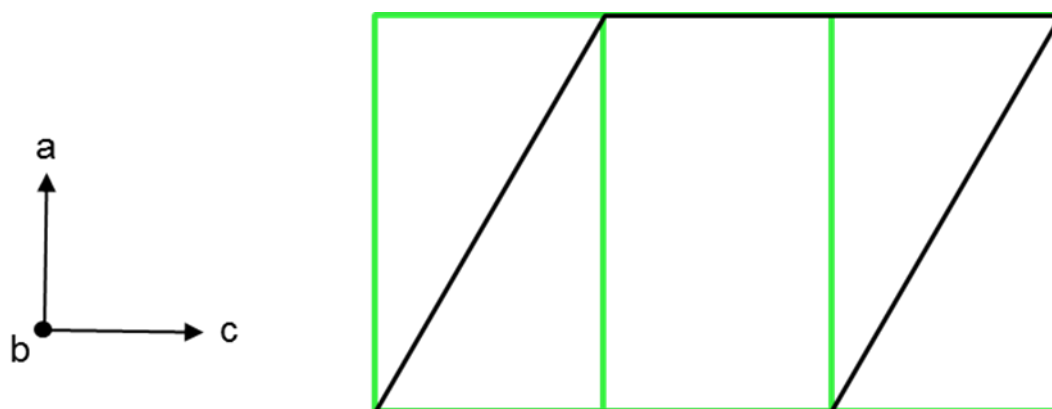


Figure 1-5 Monoclinic (black) supercell and orthorhombic (green) subcells.

The beta phase is the high temperature form of NbPO₅ that exists as the tetragonal alpha phase at the 50:50 composition in Fig. 1-6. β -NbPO₅ can be stabilized at room temperature through a rapid quenching process. In the only paper describing the electrochemical properties of this phase, Patoux achieved 90 mAh·g⁻¹ over 100 cycles to 1.85V and 120 mAh·g⁻¹ for 45 cycles to 1.7V against Li/Li⁺ at a C/5 rate.²⁵ Potentiostatic Intermittent Titration Technique (PITT) characterization revealed three intercalation plateaus during lithiation at $x = 0.2$, $0.5 \leq x \leq 0.7$, and $x = 0.8$ in β -Li_xNb_{1-x}PO₅. X-ray diffraction revealed a solid solution mechanism for the two small plateaus and a large two-phase reaction that corresponds to β -Li_{0.45}NbPO₅ and β' -Li_{0.75}NbPO₅. The second phase corresponds to a $P2_1/c$ space group (14) with $a = 13.145(3)$ Å, $b = 5.131(1)$ Å, $c = 13.415(3)$ Å, $\beta = 102.02(1)^\circ$, and $V = 783.4$ Å³. Lithiation beyond 1V generates an irreversible amorphous phase.

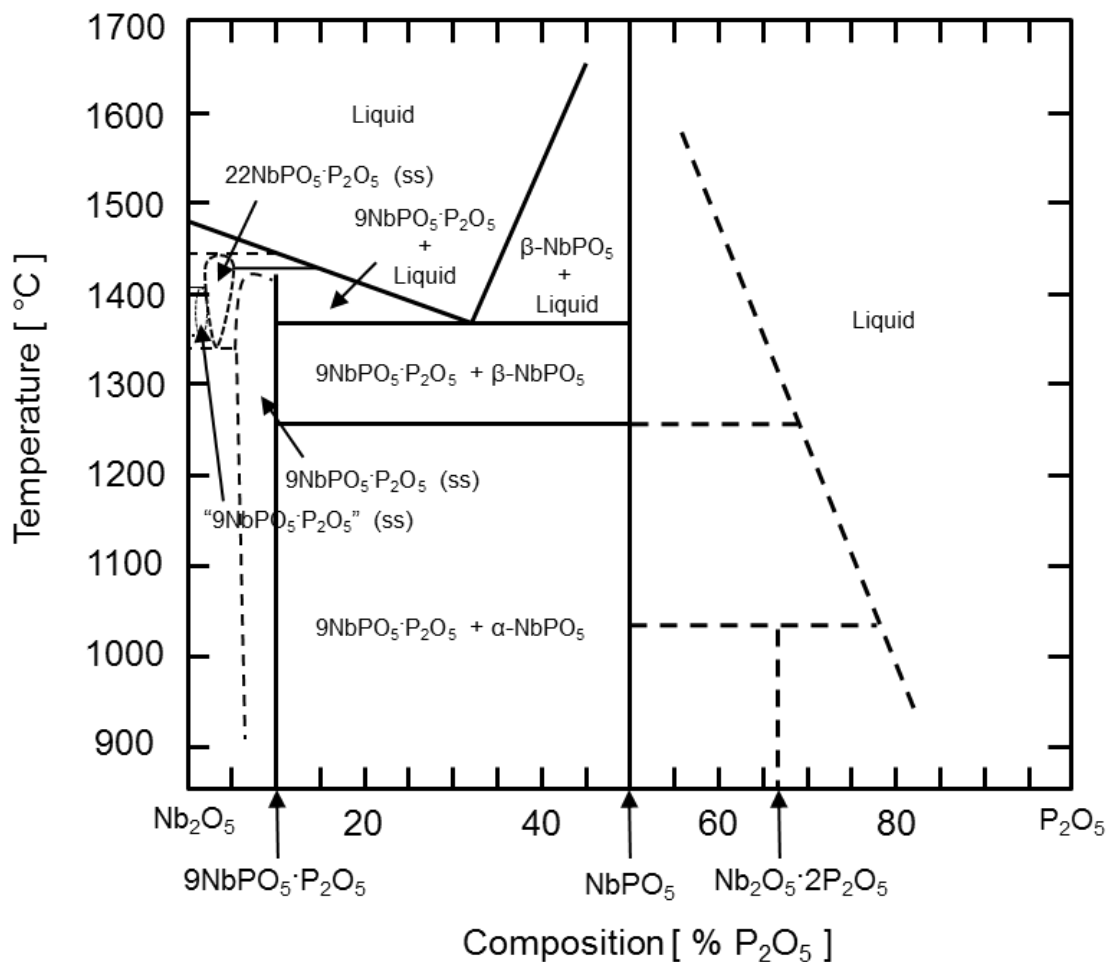


Figure 1-6 Nb_2O_5 - P_2O_5 phase diagram redrawn in part from Levin and Roth.¹⁴

Because of the intermediate 2V operating potential, $\beta\text{-NbPO}_5$ can serve as either the positive or negative electrode. In this thesis, $\beta\text{-NbPO}_5$ is tested as the positive electrode versus a lithium metal negative electrode. The flat voltage profile of $\beta\text{-NbPO}_5$ makes it an excellent candidate for a model reference material. The low irreversible loss upon charge and discharge is also accompanied by little to no change in the crystal structure after a complete cycle.

1.9 Alpha and Orthorhombic Niobium Phosphate

As seen in Fig. 1-6, several Nb-P-O phase compositions exist at different temperatures and compositions. Patoux studied the low temperature tetragonal α -NbPO₅ with the space group $P4/n$ ($Z=2$) with $a = 6.388(1)$ Å and $c = 4.118(1)$ Å, pictured in Fig. 1-7.²⁵ α -NbPO₅ is isostructural with α -VPO₅,²⁶ MoPO₅,²⁷ and VMoO₅.²⁸ To synthesize α -NbPO₅, Nb₂O₅ and a 50% stoichiometric excess of (NH₄)H₂PO₄ are mixed in a solution synthesis process and heated to 1100°C with intermittent annealing and grinding at 700°C and 950°C.

Patoux achieved 90 mAh·g⁻¹ after 50 cycles from 3.20V to 1.20V at a C/10 rate. The two-phase reaction occurs at 1.7V and shows irreversible losses over each cycle. α -NbPO₅ displays a large polarization each cycle in addition to a large 50% irreversible drop in capacity after the first cycle. With a lower operating voltage and poor reversibility, β -NbPO₅ is clearly the superior phase for electrochemical cycling.

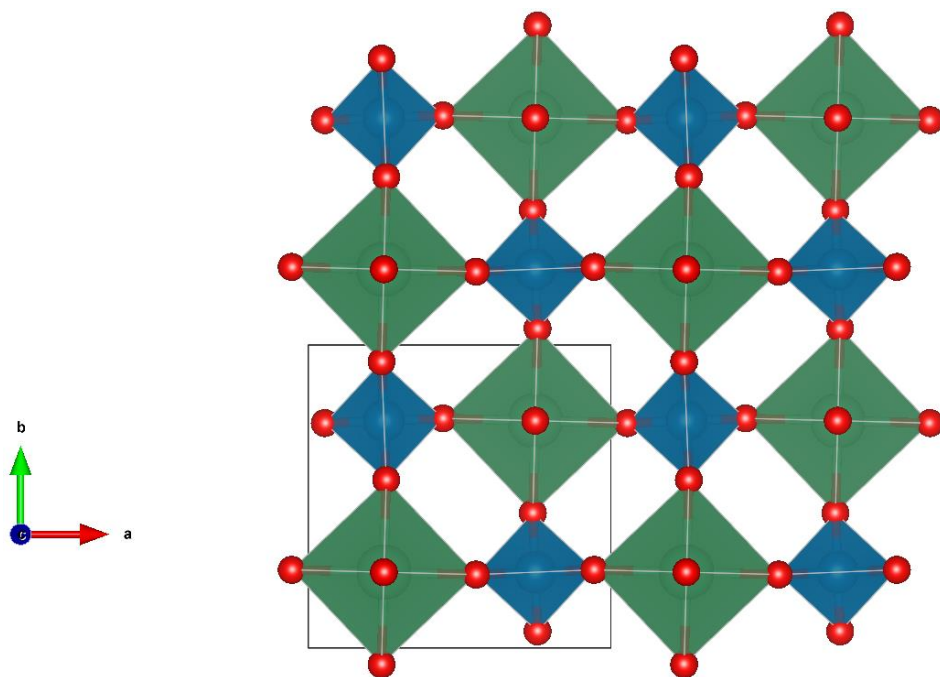


Figure 1-7 Structure of tetragonal α -NbPO₅ from the [001] direction.

During the synthesis of α -NbPO₅ and β -NbPO₅, an orthorhombic Nb_{1.91}P_{2.82}O₁₂ phase was identified after the intermediate heat treatment at 950°C. Approximately 80% purity was obtained for the orthorhombic phase with space group *Pnma* with $a = 11.304$ Å, $b = 5.316$ Å, and $c = 6.64$ Å, pictured in Fig. 1-8. The orthorhombic phase is extremely similar to the monoclinic phase, but the NbO₆ octahedra are not tilted. No literature exists detailing the electrochemical properties of this phase.

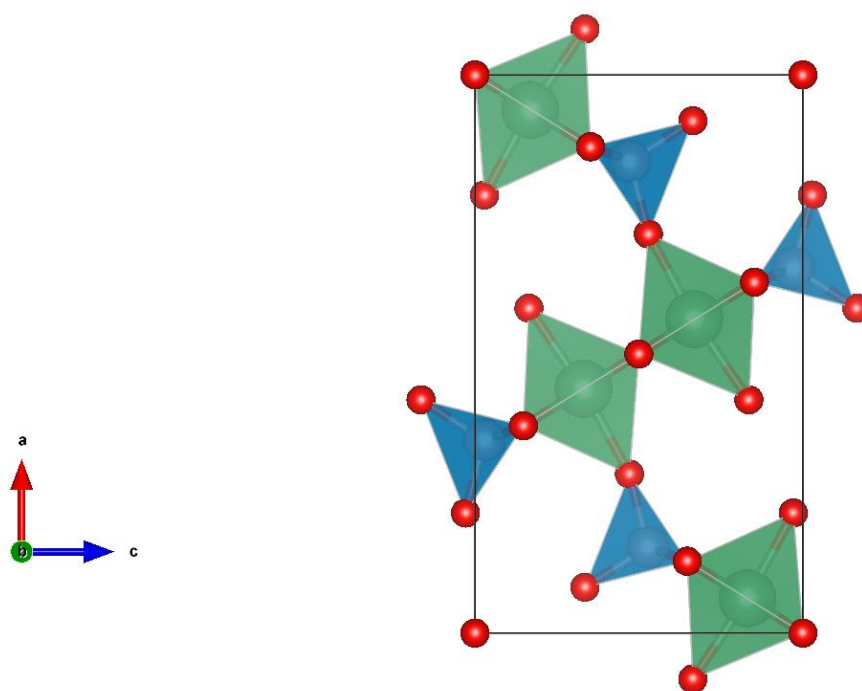


Figure 1-8 Orthorhombic unit cell shown from the [010] direction.

1.10 Ionic Substitutions

The influence of metal substitution on the reaction mechanisms and electrochemical properties of β -NbPO₅ has yet to be investigated. This thesis details the improved electrochemical performance of β -NbPO₅ through adjusting various synthesis techniques. Solid state and solution synthesis methods are used with metal ion substitutions into the β -NbPO₅ structure. Table 1-1 details transition metals that were selected based on proximity on the periodic table and similar ionic radii of coordination VI. It is of notice that Ta⁵⁺ has the same ionic radii as Nb⁵⁺ and thus was chosen as the primary ion of interest. Mo⁵⁺ was trialed and the results are detailed in chapter 3. W⁵⁺ and V⁵⁺ were also tested but did not stabilize a pure monoclinic beta phase.

Table 1-1 Ionic radii with coordination VI of selected ions.²⁹

Ion	Ionic Radius, Coordination VI [Å]
Nb ⁵⁺	0.64
Ta ⁵⁺	0.64
Cr ⁵⁺	0.63
W ⁵⁺	0.62
Mo ⁵⁺	0.61
V ⁵⁺	0.54

1.11 Research Plan

To study the niobium phosphate system, it is imperative to find an effective synthesis method. Purities greater than 95% and even 99% are desired for electrochemical testing so that there is no effect from side reactions or errors made in calculating the true specific capacities. Transition metal substitutions will be completed using high temperature anneals and adjusting the initial stoichiometric components. The resulting effects of transition metal substitutions will be examined using *ex-situ* X-ray diffraction and electrochemical characterization techniques such as galvanostatic charge-discharge cycling and Potentiostatic Intermittent Titration Technique (PITT). Beneficial results from certain substitutions will be optimized to improve the performance of β -NbPO₅.

2 Experimental

2.1 Synthesis

β -NbPO₅ and β -Ta_xNb_{1-x}PO₅ were obtained by mixing stoichiometric amounts of Nb₂O₅ (Aldrich), Ta₂O₅ (Alfa Aesar), and (NH₄)₂HPO₄ (Aldrich) in 4g batches.

Previously, Patoux²⁵ utilized a 300% stoichiometric excess of phosphorus to synthesize a pure beta phase because of volatilization of P₂O₅ at elevated temperatures. This study, however, used only 50% and 100% stoichiometric excesses and shorter anneal times for high purity (>99%) samples. Former studies employed gel-route methods,^{25,30} solution processes with HF,³¹ and high pressure techniques,³² but this study uses a facile solution synthesis with deionized water. Solid state and solution methods were tested, with solution syntheses providing more consistent and homogenous results due to a greater degree of mixing. For solid state samples, a mortar and pestle was used for grinding until homogeneous. Excess H₂O and NH₄⁺ were evolved through high temperature anneals at 700°C, 950°C, and 1350°C. Between each anneal, samples were reground to improve the effectiveness of solid state mixing. Details of heating curves are in Table 2-1.

Table 2-1 Annealing conditions.

Temperature [°C]	Heating Rate [°C·min ⁻¹]	Dwell Time [hr]	Cooling Rate [°C·min ⁻¹]
700	6	3	6
950	5	7	8
1350	8	3	11 (or quench)

For the solution synthesis, $(\text{NH}_4)_2\text{HPO}_4$ was dissolved in 5mL of deionized water (Aldrich) until saturated and then mixed with the metal oxide precursors. The slurry was spun in a 20cc fine alumina crucible on a hot plate with a magnetic spin bar. The sample was mixed and heated until the H_2O evaporated and placed directly into the furnace. The heating curves are previously detailed in Table 2-1, including quenches from 1350°C using a drop furnace that has a stage platform that lowers and exposes the sample to ambient temperatures. Previous experiments by Patoux needed a rapid quench to stabilize the $\beta\text{-NbPO}_5$ phase from the $\alpha\text{-NbPO}_5$ phase, but an air quench using the drop furnace provided sufficient cooling rates for such small samples.²⁵

Nanocomposites and mills were prepared using a Spex 8000 mill with hardened steel balls. Nanocomposites contained 10 weight percent of conductive carbon (Super P, MMM) and were milled in either dry air or helium for 15 or 30 minutes. Milling times were minimized to reduce the probability of iron contamination into the samples. Electrochemical tests revealed that milling carbon nanocomposites was unnecessary as pristine samples performed well without electron conducting additives.

Specific surface area measurements of powder samples were taken using a Micromeritics ASAP 2020 and Brunauer-Emmett-Teller theory. Samples were degassed at 120°C for at least 15 hours and subsequently analyzed with an 11 point test and nitrogen adsorbate.

Electrodes were prepared using a doctor blade process in low humidity $<0.1\%$ using the Bellcore method³³ with 54.7% active material, 7.8% conductive carbon (Super P, MMM), 15.6% poly(vinylidene fluoride-*co*-hexafluoropropylene) binder (Kynar 2801, Elf Atochem), and 21.9% dibutyl phthalate plasticizer (Aldrich) in acetone, equating to a

70 weight percent active material electrode. After casting, tapes were rinsed and extracted in 99.8% anhydrous diethyl ether (Aldrich) and punched into 1/2" disks for assembly in a helium filled glove box with $<0.1\text{ppm H}_2\text{O}$ and $<0.1\text{ppm O}_2$ content. Cells were cycled against a lithium metal anode (FMC) in a 2032 Al clad coin cell (Hohsen) with 1M LiPF_6 EC:DMC 1:1 (BASF) electrolyte and GF/D glass fiber separator (Whatman).

2.2 X-ray Diffraction

X-ray Diffraction (XRD) is a keystone structural characterization tool used by materials scientists, chemists, and physicists alike to identify the crystallographic structure of materials. Also known as X-ray crystallography, this technique was first introduced by Max von Laue in 1912. Broadly, XRD uses a solid or powder sample and directs X-rays at the sample to measure the constructive interference of the diffracted beam. A diffraction pattern is obtained and the peak positions and relative intensities can be compared with existing patterns in the ICDD database to determine the phases present.

X-rays are a form of electromagnetic radiation with wavelengths ranging from 0.5 to 2.5 angstroms. This size is optimal for Bragg diffraction because these wavelengths are on the same order of magnitude as atomic radii. Smaller wavelengths are more difficult to generate and focus, while larger wavelengths result in worse resolution. To generate a monochromatic X-ray beam, in this case Cu K_{α} , a several steps are taken. A large potential is run through a high resistance tungsten filament, heating it up and boiling off electrons once the thermal energy overcomes the work function of tungsten. These electrons escape into a vacuum and are driven towards a copper target by an applied electric potential. When the electrons strike copper, characteristic and Bremsstrahlung, or braking radiation is produced.

Characteristic X-rays are generated when an incoming high energy electron strikes a low energy electron that gets ejected from an inner shell in the atom. This ejection leaves behind a vacancy, allowing another higher shell electron to relax into this position. This relaxation generates an X-ray of a characteristic energy.

Bremsstrahlung or braking radiation is generated when an electron passes by the nucleus of an atom and is slowed down and changes its path. This loss of energy results in X-rays of variable energy. Braking radiation accounts for the majority of the X-rays generated, however, a monochromatic X-ray beam is needed to calculate the d-spacing. To do so, a filter is added to allow only the Cu K_α X-rays to travel through. In general, a filter material is one position to the left of the target material on the periodic table. In the case of Cu ($Z=29$), a Ni ($Z=28$) filter is used. As seen in Fig. 2-1, the Ni absorption edge falls between the Cu K_α and Cu K_β wavelengths. The Ni filter absorbs the Cu K_β and braking radiation, leaving behind a monochromatic Cu K_α X-ray beam.

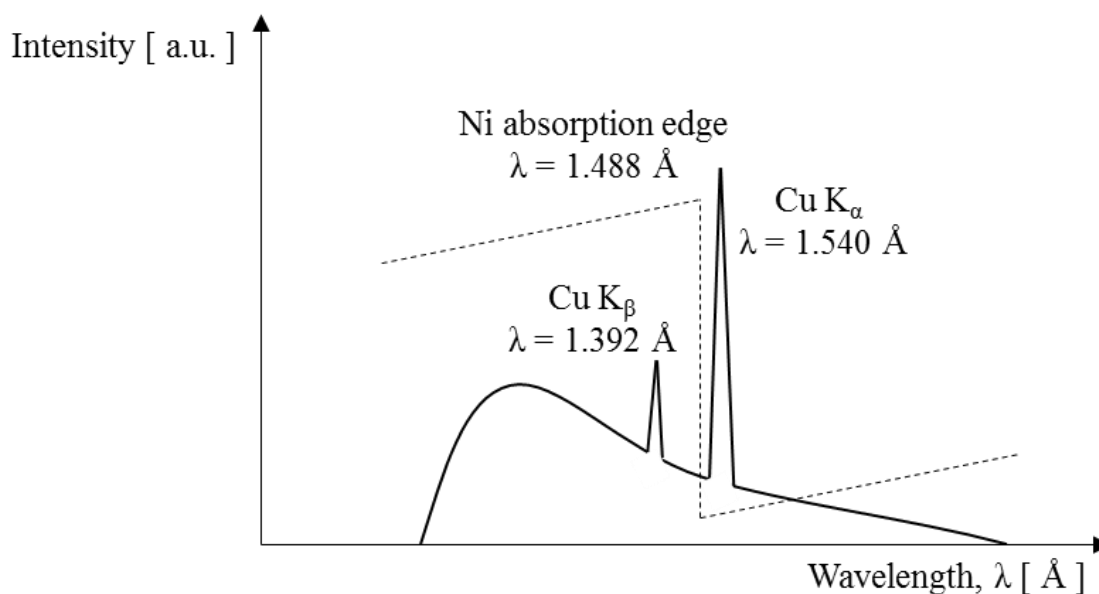


Figure 2-1 X-ray spectrum of characteristic and braking radiation with a Cu target and Ni filter.

Now a monochromatic beam, the X-rays pass through a soller collimator so that only the parallel radiation passes through. When the X-rays strike the sample, they interact with the electron clouds of the atoms and scatter in all directions. Other interactions occur, such as the ejection of Auger and backscattered electrons, but only X-rays at the specified 2θ angle are detected. With known values for the wavelength of the X-ray and the 2θ angle, it is now possible to calculate the d-spacing through Bragg's Law where n is an integer, λ is the wavelength of the X-ray, d is the d-spacing, and θ is the incident angle.

$$n\lambda = 2d \sin \theta \quad (\text{Eq. 3})$$

In other words, when the extra distance traveled by an X-ray ($2d \sin \theta$) is an integer multiple of the wavelength of the X-ray, constructive interference occurs and will show up as a peak located at a specific 2θ in the diffraction pattern. This concept is demonstrated in Fig. 2-2 where the black circles are the atoms in the gray lattice planes and the red lines are the incident X-rays.

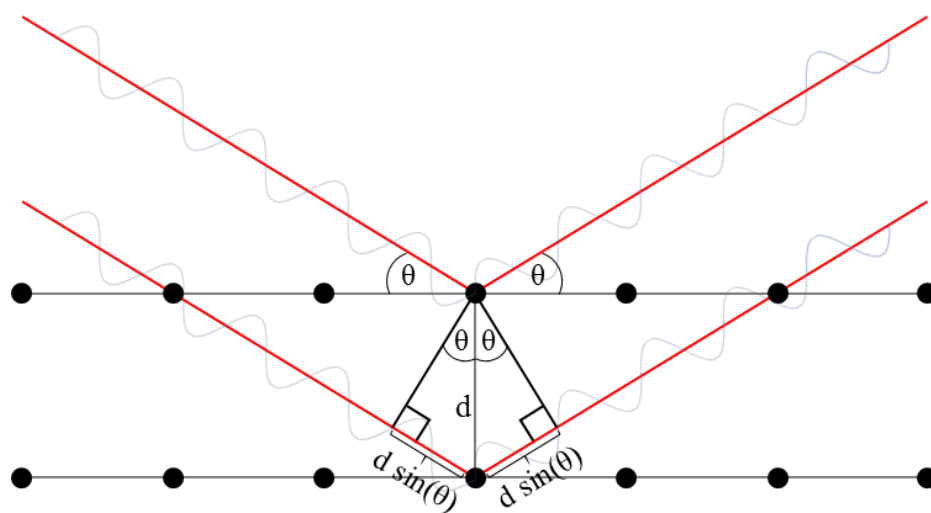


Figure 2-2 Illustration of Bragg's Law.

The entire concept of X-ray diffraction is dependent on the fact that many materials have a periodic crystal structure. The long-range order entails that there will be another plane that is exactly out-of-phase causing complete destructive interference and thus no intensity measured. However, this assumes a perfect crystal and perfect crystals do not exist in nature. There are several factors that can affect the intensities, peak positions, and peak shapes in the final diffraction pattern, namely the structure, polarization, multiplicity, Lorentz, absorption, and temperature factors. Of these, the structure factor plays the largest role because it affects the presence or lack of certain reflections of the unit cell. It is important to understand the effects of these parameters when modeling using Rietveld techniques to obtain a good fit.

Furthermore, the sample itself can produce different effects on the diffraction pattern. For example, an amorphous sample with no long range order will not produce sharp peaks, and any short-range order will show broadened peaks with lower intensities. If samples have very small crystallite sizes, the peaks will broaden whereas large bulk samples will produce greater intensities with less broadening. Peak broadening is also observed from the previously mentioned factors such as the temperature factor. Thermal energy causes atoms to vibrate which slightly alters the d-spacing of the lattice planes, thus broadening the peaks.

For this thesis, powder samples were characterized using a Bruker D8 Advance diffractometer with $\text{Cu K}_{\alpha 1} = 1.54056\text{\AA}$ and $\text{Cu K}_{\alpha 2} = 1.54443\text{\AA}$. The 2θ values ranged from 15° to 60° and scans were run with a 0.02° increment and either 0.5, 0.75, or 3 second per increment scan speed. *Ex-situ* measurements of solid electrodes were also taken using the same diffractometer and scan conditions. Samples were prepared by

disassembling cells in a helium environment to extract the cycled electrodes. These electrodes were rinsed in DMC to remove lithium salt crystals and were dried before sealing on a glass slide using Kapton film and synthetic grease to prevent oxidation and moisture contamination. Phases were analyzed using EVA software and then matched to the ICDD database.

2.3 Rietveld Refinement

Experimental diffraction peaks can be modeled using a technique named after Hugo Rietveld who developed the method in 1969. Rietveld analysis requires several different instrumental and sample specific parameters to create a theoretical diffraction pattern. The calculated pattern is then compared to the experimental pattern using a least squares regression. The difference plot is minimized by tuning different parameters and when a low goodness of fit (GOF) or chi-squared (χ^2) value is obtained, the fit has improved. There is no perfect fit, so patterns are improved by monitoring the GOF and χ^2 values and most importantly by using the human eye to determine how well a model fits the experimental pattern. There are no requirements for GOF or χ^2 values to indicate a good fit, and it is much more important to see that the model is accurate by eye. A pattern with a lot of background noise can be fit with a low GOF or χ^2 value while simultaneously having incorrectly modeled peak shapes due to the nature of how a least squares regression is calculated.

Rietveld refinements were performed using TOPAS software with a 5th order Chebychev polynomial fit for the background and a Bragg-Brentano geometry setup. A pseudo-Voigt peak shape was assumed with sample height displacement and atomic positions refined. No corrections were added for the conductive carbon and binder additives because they did not appear in the diffraction pattern. 3D models and images were generated using VESTA software.

2.4 Galvanostatic Cycling and Rate Protocols for Half Cells

Batteries are prepared as half cells where the niobium phosphate electrode is prepared against a lithium metal negative electrode. These half cells are cycled galvanostatically, which is where the current is controlled and the voltage is measured. Cutoff voltages are set for discharge and charge and the cell cycles within this range. A current (mA) is determined based off of the specific current ($\text{mA}\cdot\text{g}^{-1}$). When current is described as 1C, this means that the cell will discharge in 1 hour. A 0.5C or C/2 rate is half the rate, or a 2 hour discharge, whereas a 2C rate is a 30 minute discharge. Typically, the specific capacity ($\text{mAh}\cdot\text{g}^{-1}$) is measured each cycle and is plotted as a function of the number of cycles.

To test the rate capabilities of a cell, the cell is subject to a higher load during charge and the subsequent discharge is completed at a slow rate to reveal the effect of the increased charging rate on the discharge capacity. At higher charging rates, the cell exhibits lower discharge capacities due to kinetic and thermodynamic limitations. For example, if a cell demonstrates a reversible drop in capacity after being subject to high rates, then it is kinetically limited. Through high resolution electrochemical techniques, it can be determined what mechanisms cause the drop in capacity.

2.5 Potentiostatic Intermittent Titration Technique

High resolution electrochemical techniques are necessary to examine the operation mechanisms in greater detail. Potentiostatic Intermittent Titration Technique (PITT) is an excellent method for this as it gives insight to the reaction mechanisms with great precision as it forces the reaction to proceed slowly to remain near equilibrium. In PITT, the potential is held constant while the current is monitored, and the reaction does not proceed until a certain cutoff current is reached. The cell reaction will not proceed to the next voltage step unless it is thermodynamically and kinetically favorable. The current response to a small negative voltage step is illustrated on the left in Fig. 2-3 and the right shows a small positive voltage step. On discharge, a negative potential step causes a decrease in current and the voltage is held until the current decays back to zero. The opposite is true during charge where a small positive potential step causes a positive current response that decays to zero. For practical matters, a cutoff current or time is added so that the test proceeds to the next step in a reasonable amount of time.

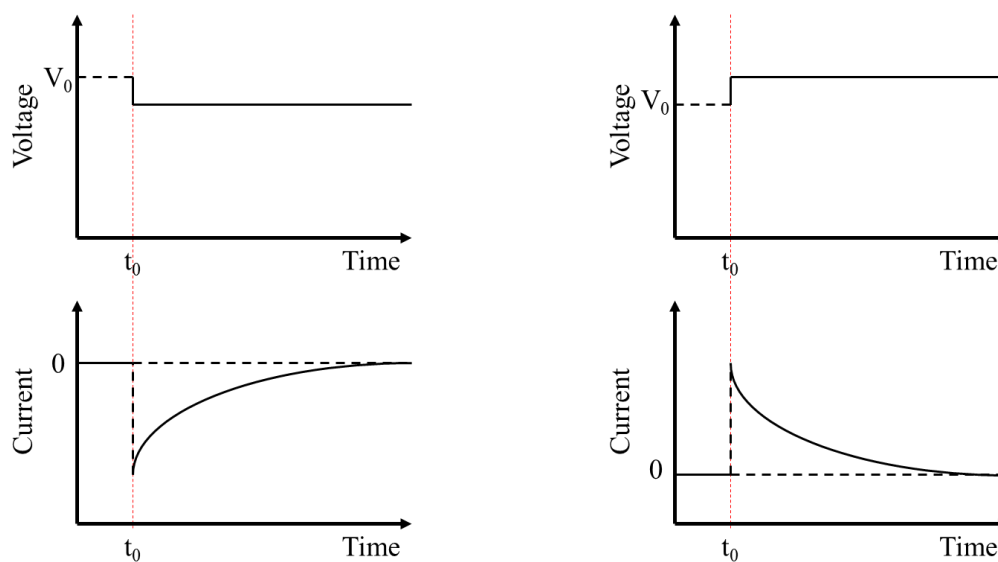


Figure 2-3 Current response to a small negative (left) and positive (right) potential step change.

Using PITT, the diffusion coefficient can also be calculated from the linear portion of the Cottrellian region ($1/t^{1/2}$ dependence) using Eq. 4 where D_{Li^+} is the diffusion coefficient of Li^+ , I is the current, t is time, and L is the diffusion length.³⁴

$$D_{Li^+} = -\frac{d \ln I}{dt} \frac{4L^2}{\pi^2} \quad (\text{Eq. 4})$$

For PITT, several assumptions are made for the calculations to hold true.³⁵

- 1.) One-dimensional semi-infinite particles are large enough so that size effects are insignificant.
- 2.) Fickian dynamics follow Fick's equation for transport with no gradient energy term.
- 3.) Constant diffusion coefficient as the concentration changes during a single voltage step.
- 4.) Cutoff current that allows for infinite time integration that is cutoff after some reasonable time interval.
- 5.) Small enough voltage step for the previous assumptions to be held.
- 6.) No current response from dynamics outside the particle.

3 Investigation of Physical and Electrochemical Properties of β -Ta_xNb_{1-x}PO₅ as an Electrode for Lithium Batteries

3.1 Results

3.1.1 Structure

To evaluate the optimum synthesis methodology, samples were synthesized using the aforementioned solid state and solution methods along with quenching from various temperatures. After heating at 1350°C, unsubstituted samples were either immediately quenched or slowly cooled to 300°C before quenching in air. Fig. 3-1 shows the XRD patterns. All samples, except for the solid state sample quenched from 300°C, displayed 100% purity of the monoclinic β -NbPO₅. This was most likely due to a greater degree of inhomogeneity in the precursor mix. Based on the improved purities, all reported samples were synthesized through a solution technique and quenched from 1350°C unless otherwise specified.

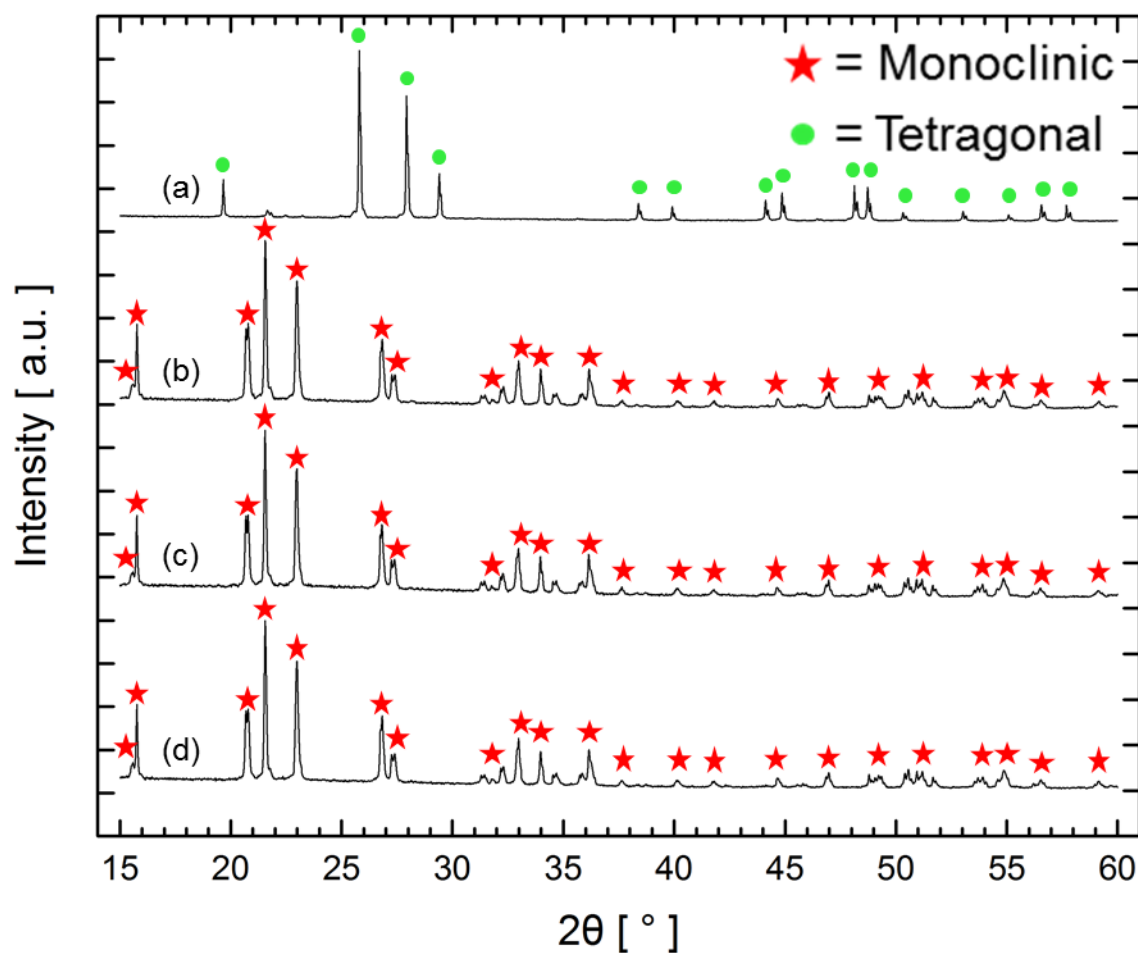


Figure 3-1 XRD patterns for NbPO_5 synthesized using solid state methods with quenching from 300°C (a) and 1350°C (b), and solution methods with quenching from 300°C (c) and 1350° (d). Circles indicate the tetragonal $\alpha\text{-NbPO}_5$ phase and stars indicate the monoclinic $\beta\text{-NbPO}_5$ phase.

Previous studies by Patoux,²⁵ Chahboun,¹⁵ and Levin¹⁴ all indicate that a large excess of phosphorus was needed to produce a pure phase. Haider³⁶ reported that P_2O_5 volatilizes at 1070°C, which is much lower than the temperature required to form the high temperature monoclinic phase. However, it was discovered that shortening the anneal times minimizes the amount of phosphate evolution and only a 50% stoichiometric excess of phosphorus was needed to yield >99% purity. Table 3-1 details the purity of samples containing varying amounts of excess phosphorus heated to 1350°C and quenched at 1350°C.

Table 3-1 Composition of 4g batches containing varying amounts of excess phosphorus.

Excess Phosphorus	$\beta\text{-NbPO}_5$	$P_2O_5 \cdot 9Nb_2O_5$
0%	87.1%	13.9%
50%	100%	0%
100%	100%	0%

A range of quenching temperatures were tested for both unsubstituted and 2% Ta substituted samples and their subsequent purities are reported in Table 3-2. The addition of 2% Ta stabilized a pure Beta phase at quenches starting from as low as 200°C, which is in contrast to previous attempts needing extremely rapid quenches above 1300°C.^{25,32}

Table 3-2 Purity of 0% and 2% Ta samples quenched from different temperatures.

0% Ta			2% Ta		
Quench Temperature	$\alpha\text{-NbPO}_5$	$\beta\text{-NbPO}_5$	Quench Temperature	$\alpha\text{-NbPO}_5$	$\beta\text{-NbPO}_5$
200°C	17.0%	83.0%	200°C	0%	100%
300°C	0%	100%	300°C	0%	100%
400°C	0%	100%	400°C	0%	100%
500°C	0%	100%	500°C	0%	100%
1350°C	0%	100%	1350°C	0%	100%

The X-ray patterns for Ta substitutions ranging from 0% to 100% prepared at 1350°C and subsequently quenched at 1350°C are shown in Fig. 3-2. All Bragg reflections can be indexed to the monoclinic unit cell of the Beta phase and only very small amounts of secondary phases were present. Lattice refinements reveal that the unsubstituted NbPO₅ is in good agreement with the literature value for the monoclinic space group $P2_1/c$ ($Z=8$) of $a = 13.0969(16)$ Å, $b = 5.2799(6)$ Å, $c = 13.2281(16)$ Å, and $\beta = 120.334(8)^\circ$.³⁷ All of the β -Ta_xNb_{1-x}PO₅ samples were analyzed using Rietveld analysis with results presented in Table 3-3. The 10% and 20% Ta samples required a larger 100% stoichiometric excess of phosphorus to yield higher purity with <5% P₂O₅·9Nb₂O₅ present as an impurity phase. Higher amounts of excess phosphorus were tested, but resulted in samples fusing to the crucible during heat treatments. The lattice parameters present no significant or systematic change with increasing amounts of Ta substitution, only a maximum 0.17% change in the volume from 0% to 100% substitution. The ionic radii of Nb⁵⁺ and Ta⁵⁺ are nearly identical at 0.64 nm²⁹ and thus the invariant result is consistent with Vegard's law.

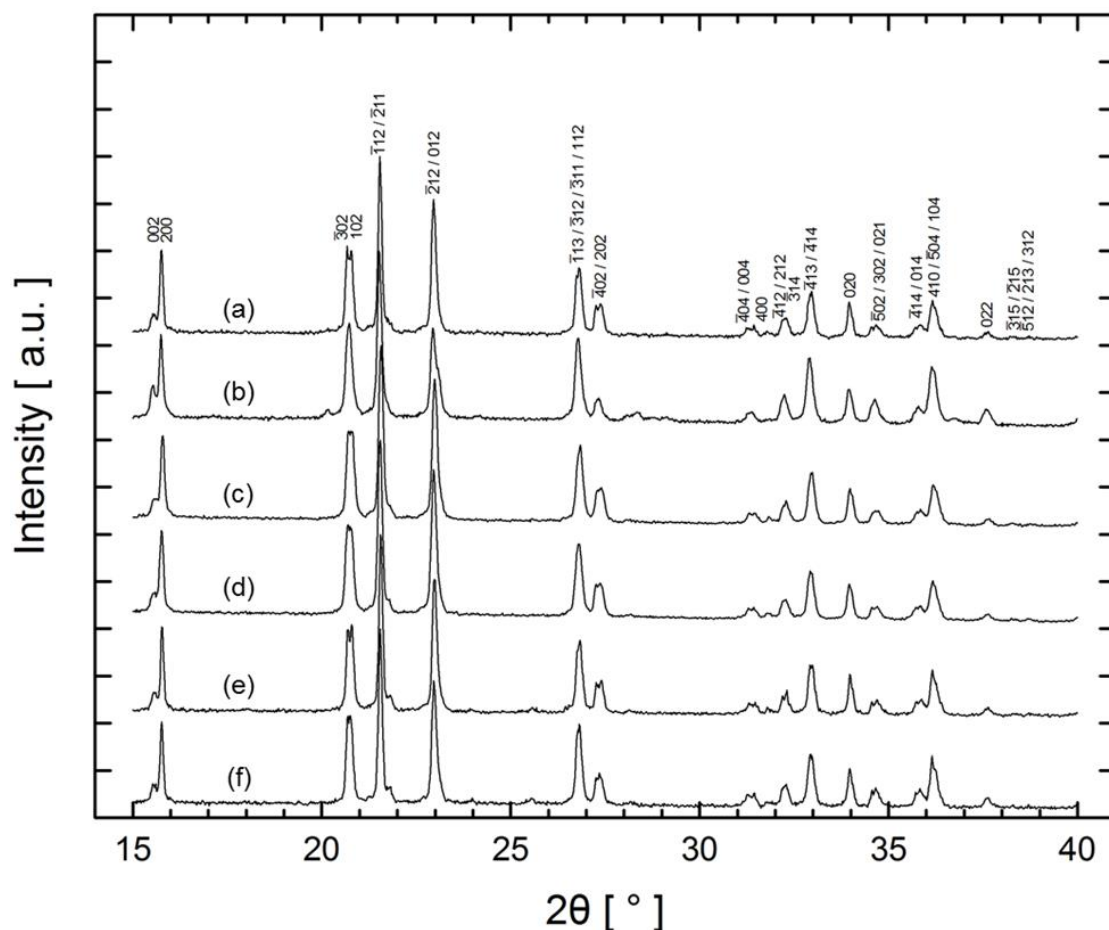


Figure 3-2 XRD patterns for various percentages of Ta⁵⁺ substitution in Ta_xNb_{1-x}PO₅ quenched at 1350°C: (a) 0%, (b) 2%, (c) 5%, (d) 10%, (e) 20%, and (f) 100% Ta. Miller indices are given for the monoclinic Beta phase.

Table 3-3 Rietveld refinement data for various molar % Ta substitutions for Nb in NbPO₅. All samples were quenched from 1350°C.

% Ta	Wt %	R _{exp}	R _{wp}	R _p	GOF	a [Å]	b [Å]	c [Å]	Beta [°]	Volume [Å ³]
0	100.0	6.86	8.78	6.89	1.28	13.08(4)	5.27(7)	13.22(6)	120.68(1)	785.45(7)
2	100.0	4.35	5.83	4.53	1.34	13.08(7)	5.27(9)	13.23(4)	120.69(2)	786.40(3)
5	100.0	4.43	6.24	4.87	1.41	13.08(5)	5.27(8)	13.23(0)	120.69(3)	785.82(2)
10	96.8	6.29	8.05	6.20	1.28	13.08(7)	5.27(7)	13.22(4)	120.66(1)	785.77(4)
20	95.1	6.23	7.98	6.24	1.28	13.08(1)	5.27(6)	13.22(7)	120.64(7)	785.54(3)
100	100.0	3.87	5.92	4.51	1.53	13.03(3)	5.27(9)	13.24(1)	120.27(9)	786.81(5)

3.1.2 Electrochemistry

The $\text{Ta}_x\text{Nb}_{1-x}\text{PO}_5$ compositions were slowly cycled against a lithium metal anode in 1M LiPF_6 (EC:DMC 1:1) at $7.5 \text{ mA}\cdot\text{g}^{-1}$ (C/12 – C/15) to obtain the voltage profiles of the 1st and 75th cycles shown in Fig. 3-3. The specific capacities upon the first lithiation and delithiation are tabulated in Table 3-4. The experimental data show a reasonable and systematic agreement with the theoretical specific capacity with most samples within 85-90% of theoretical capacity. Interestingly, the samples demonstrate exceptionally low loss of <1% between the first lithiation and delithiation. The voltage profile associated with the Li^+ insertion process systematically evolves as a function of Ta substitution. This is most apparent in the second half of the voltage profile where the profile develops an increasing slope and lower polarization/hysteresis with increasing Ta substitution. From these voltages profiles, it becomes clear that increasing amounts of Ta result in a more sloped voltage profile of lower polarization while also decreasing the discharge capacity—as expected from the increase in molecular weight.

Table 3-4 Discharge capacities of the first cycle at $7.5 \text{ mA}\cdot\text{g}^{-1}$ from 2.8 V to 1.75 V.

% Substitution	Theoretical Specific Capacity [$\text{mAh}\cdot\text{g}^{-1}$]	1 st Lithiation [$\text{mAh}\cdot\text{g}^{-1}$]	1 st Delithiation [$\text{mAh}\cdot\text{g}^{-1}$]	Coloumbic Efficiency
0	131.46	111.25	111.82	100.5%
2	127.73	110.29	109.60	99.4%
5	122.25	113.65	113.55	99.9%
10	113.42	91.556	92.501	101.0%
20	96.81	79.632	78.865	99.0%

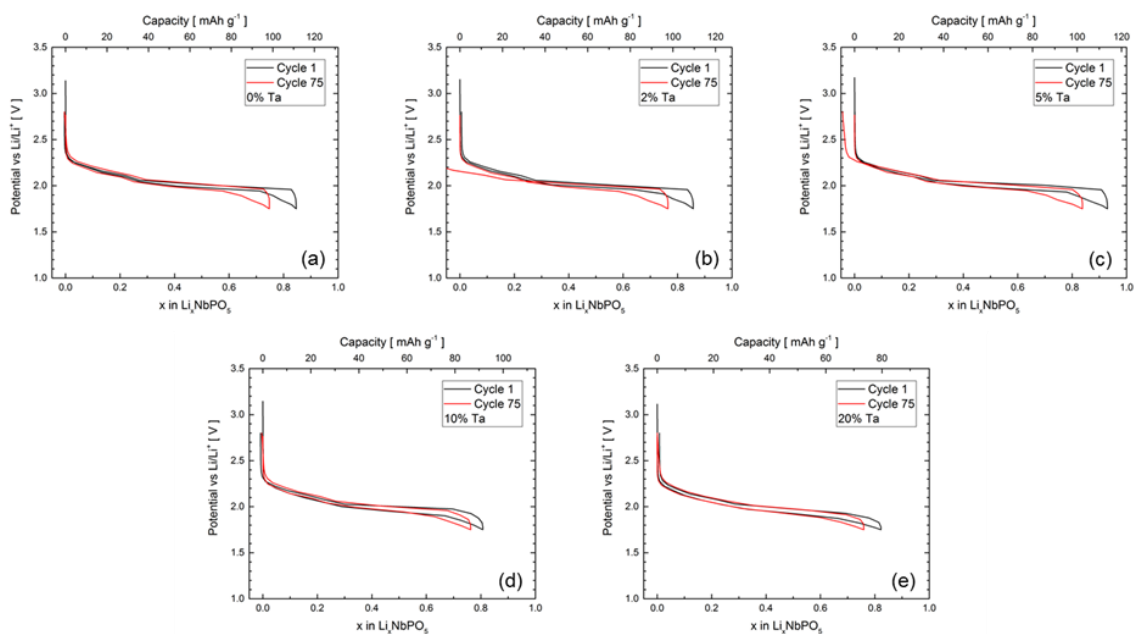


Figure 3-3 1st and 75th discharge profiles for (a) 0%, (b) 2%, (c) 5%, (d) 10%, and (e) 20% Ta substitutions at 7.5 mA·g⁻¹ from 2.8V to 1.75V.

The rate capabilities of $\text{Ta}_x\text{Nb}_{1-x}\text{PO}_5$ cells with $x = 0, 0.02, 0.05, 0.10$, and 0.20 were evaluated up to rates of $2100 \text{ mA}\cdot\text{g}^{-1}$ (19C-26C) and then subjected to continued cycling at $22.5 \text{ mA}\cdot\text{g}^{-1}$ (C/5-C/4) using the same voltage range of 2.8V to 1.75V. Fig. 3-4 shows the percent capacity retention from the first cycle (a) and the rate capabilities (b). Up to 60% utilization was observed at approximately 20C rate. No negative effects on the rate capability were observed from higher amounts of Ta substitution. However, when monitoring the percentage capacity retention as a function of cycle number, a notable improvement was seen by increasing Ta substitutions in Fig. 3-4. The improved cycling is also represented in Fig. 3-3 where larger amounts of Ta substitution result in greater stability of the voltage profile after 75 cycles.

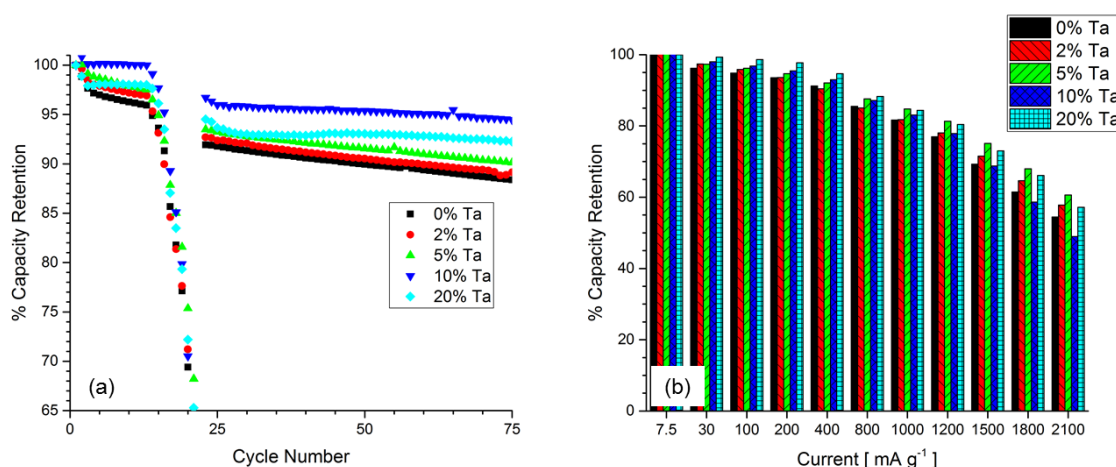


Figure 3-4 Percent capacity retention for Ta substitutions at $22.5 \text{ mA}\cdot\text{g}^{-1}$ (a). Capacity drop from cycles 13 to 21 are due to the increase in current from rate testing. Percent capacity retention for Ta substitutions at high currents (b) all cycled from 2.8V to 1.75V.

The voltage profile of the unsubstituted NbPO_5 sample suggests a possible deleterious reaction occurring at voltages $<1.8\text{V}$. To test such theory, various discharge cutoff voltages were tested for the unsubstituted sample and their voltage profiles are overlaid in Fig. 3-5a and the percentage capacity retention as a function of cycle number in Fig. 3-5b. All cutoff ranges experienced good cycling efficiency with $>90\%$ retention after 50 cycles. However, a systematic improvement in cycling efficiency is clearly seen as the discharge cutoff voltage is raised with a marked improvement for 1.75V and an especially dramatic improvement for the 1.85V cutoff. The latter exhibited approximately 3% loss after 100 cycles. The improvement in cycling stability is consistent with the avoidance of the anomaly in the voltage profile below 1.8V that was previously discussed.

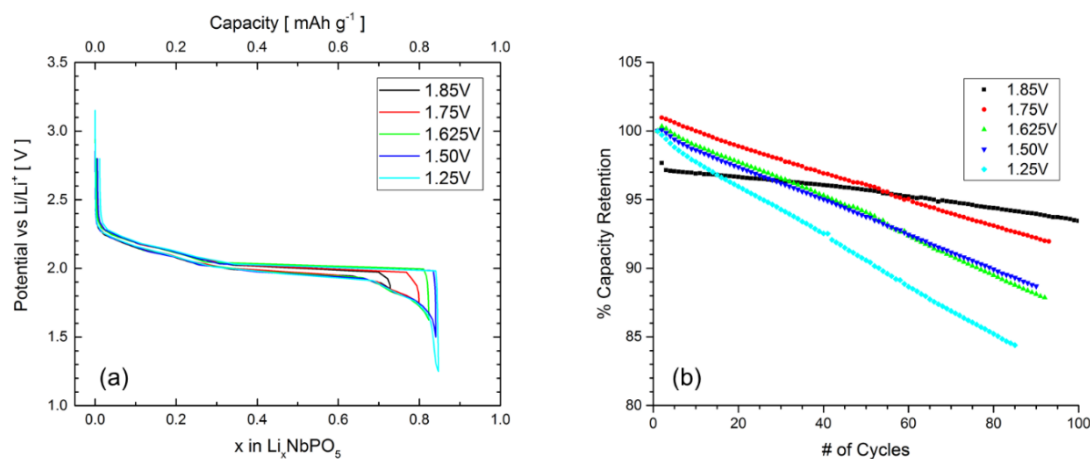


Figure 3-5 First cycle for 0% Ta samples cycled down to different cutoff voltages with a $7.58 \text{ mA} \cdot \text{g}^{-1}$ current (a) with discharge capacity retention during extended cycling (b).

Fig. 3-6 presents the effects on the voltage profile after 85 cycles at different lower voltage cutoffs. It can be clearly seen that the voltage feature $<1.8\text{V}$ led to a considerable increase in polarization that affected the entire voltage profile, as was especially seen for the 1.25V cutoff. When this feature was avoided, the polarization increase was minimal or non-existent, similar to the effect of increasing Ta substitutions.

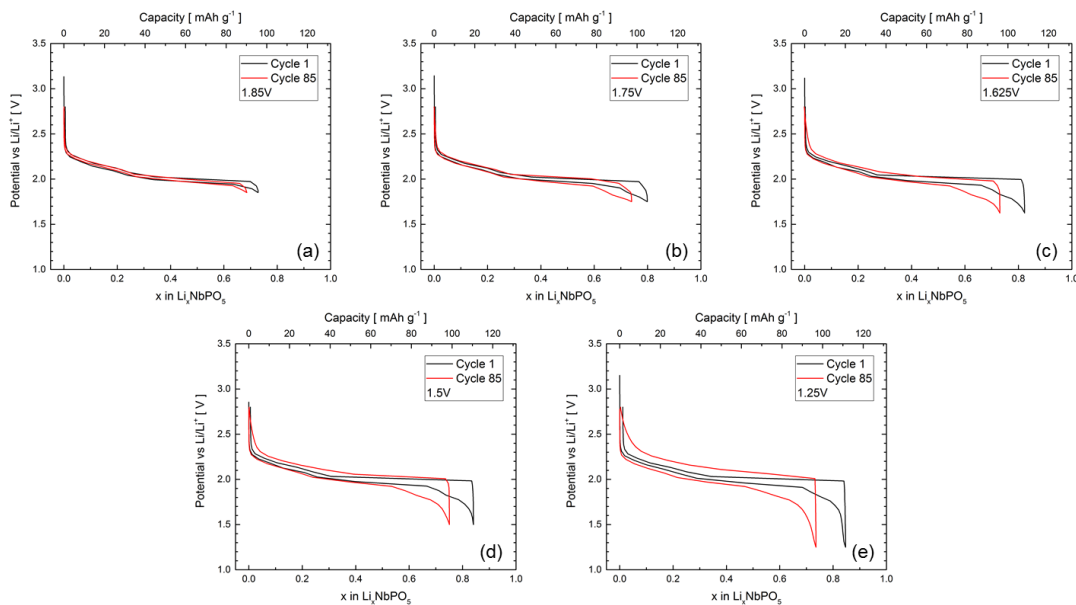


Figure 3-6 1st and 85th cycle voltage profiles for different cutoff voltages: (a) 1.85 V , (b) 1.75 V , (c) 1.625 V , (d) 1.5 V , and (e) 1.25 V .

The improved cycling efficiency obtained from changing the cutoff voltage to 1.85V is compared to the cycling stabilities of various Ta substitutions in Fig. 3-7. All of the Ta substitutions display an improvement in cyclability over the 0% unsubstituted sample with the standard 1.75V cutoff. The samples with 2%, 5%, and 10% substitutions show cycling retention on par with that of the 0% sample cycled at the higher voltage cutoff of 1.85V.

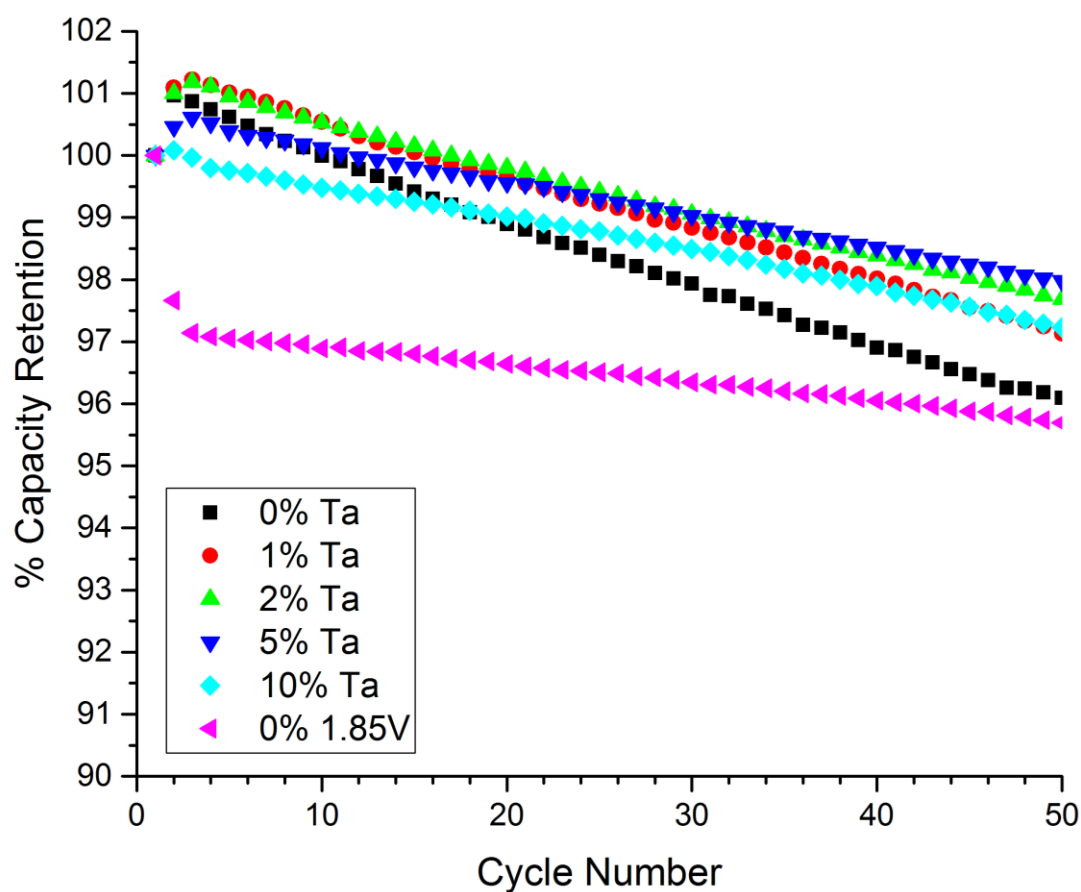


Figure 3-7 0-10% Ta substitutions cycled from 2.8V-1.75V and an unsubstituted sample cycled from 2.8V-1.85V.

To further investigate the effects of Ta substitution, the isostructural β -TaPO₅ was synthesized and cycled against a lithium metal anode. To the best of our knowledge the electrochemical activity of β -TaPO₅, representing the end member of the substitution series, has yet to be investigated. Because TaPO₅ operates on the Ta⁵⁺/Ta⁴⁺ reduction/oxidation around 1.25V, much lower than Nb⁵⁺/Nb⁴⁺, the cell's discharge cutoff voltage was tested at 1V, 0.75V, and 0.075 V (Fig. 3-8) using 316 stainless steel coin cell parts to prevent the formation of lithium aluminum alloys at low voltages. It is clear that although isostructural, β -TaPO₅ does not exhibit the reversibility of β -NbPO₅. Upon the first lithiation, there is a large irreversible transformation followed by a solid solution insertion process with a large hysteresis. The data suggests that at sufficiently low voltages a conversion process may result, but further investigation is outside the scope of this thesis. With respect to the context of the thesis, these results make it reasonable that the Ta rich Beta phases do not have any intrinsic capacity in the voltage ranges explored for the Ta substituted β -NbPO₅ materials.

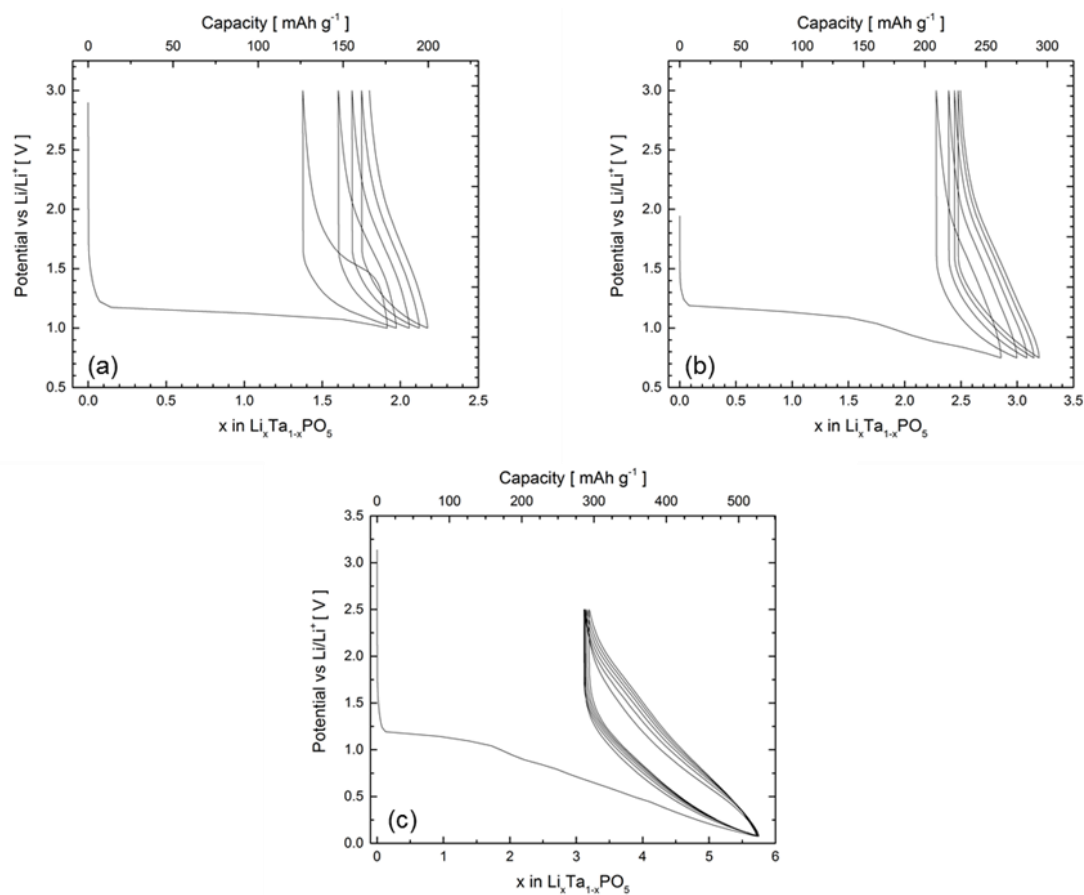


Figure 3-8 Voltage profiles for TaPO_5 from 3V to 1V (a) and 3V to 0.75V (b) both at $7.58 \text{ mA} \cdot \text{g}^{-1}$, and 2.5V to 0.075V at $10 \text{ mA} \cdot \text{g}^{-1}$ (c).

3.2 Discussion

3.2.1 Electrochemistry

Two electrochemical results presented in this manuscript are quite striking. First, the data shows a distinct improvement in already proficient cycling stability and a decrease in polarization with cycle number when the lower voltage region of the unsubstituted β -NbPO₅ <1.8V is avoided. Second, an analogous improvement of cycling and a decrease of polarization with cycle number is demonstrated by increasing Ta⁵⁺ substitution for Nb⁵⁺. The voltage profiles of the latter with increasing substitutions of Ta also systematically decrease the apparent presence of the aforementioned low voltage reaction. The connection between the presence of the lower voltage reaction and the presence of Ta are quite clear, but to confirm the lower voltage reaction mechanism was indeed evolving with Ta substitution, high resolution electrochemical techniques were utilized.

PITT experiments were run to obtain insight on the reaction mechanisms occurring for the unsubstituted samples as a function of voltage cutoff and Ta substitution. Lower voltage cutoffs of 1.85V, 1.60V, and 1.25V were tested for both the unsubstituted and substituted samples and are shown in Fig. 3-9. The PITT current response for the first lithiation of all the samples, as expected, were similar. In contrast, during delithiation of the unsubstituted sample, a clear non-Cotrellian reaction of increasing current followed by decreasing current corresponds with the flat voltage segment of the delithiation and a distinct indication of a multiphase reaction. This two phase behavior during delithiation of the unsubstituted sample is apparent for the samples limited to a 1.60V and 1.25V cutoff, but definitively absent for the 1.85V cutoff. This

suggests that the lower voltage feature below 1.8V present on the lithiation induces the multiphase reaction observed during delithiation. This behavior is completely consistent with the improved electrochemistry exemplified by improved cycling stability and lower evolution of polarization shown for samples that were limited to a 1.85V cutoff.

Interestingly, the specific capacity represented by the multiphase delithiation reaction is in far excess of the specific capacity associated with the lower voltage lithiation reaction avoided by the 1.85V PITT cutoff. In all cases, the latter part of the delithiation seems to progress in a single phase or near single phase reaction.

Fig. 3-9 unambiguously shows that increasing Ta substitution decreases and eliminates the multiphase reaction occurring on delithiation replicating the effect of increasing the cutoff voltage in the unsubstituted sample. This is clearly apparent in both the 1.60V and 1.25V cutoff.

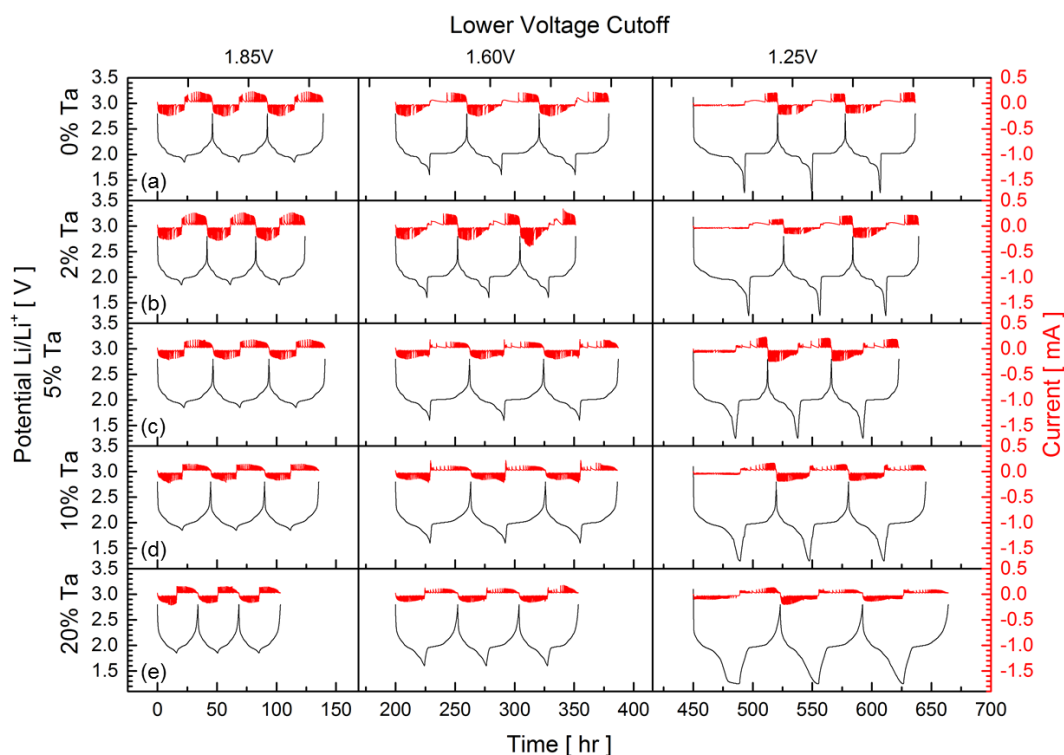


Figure 3-9 PITT results for 0% (a), 2% (b), 5% (c), 10% (d), and 20% (e) Ta to different cutoff voltages with a 10mV step and $2\text{mA}\cdot\text{g}^{-1}$ current cutoff.

To confirm that the multiphase reaction depletion was a result of Ta substitution, a similar PITT study was executed with 5% and 10% Mo substitutions into NbPO_5 using the same synthesis techniques with MoO_3 (Aldrich) to achieve 100% purity (50% stoichiometric excess of phosphorus). All phases were X-ray pure suggesting solid solution behavior. As seen in Fig. 3-10, the two phase reaction during delithiation is present at all voltage cutoffs with nearly identical PITT results as the unsubstituted sample. Thus, there is a clear benefit induced by the Ta substitution specifically.

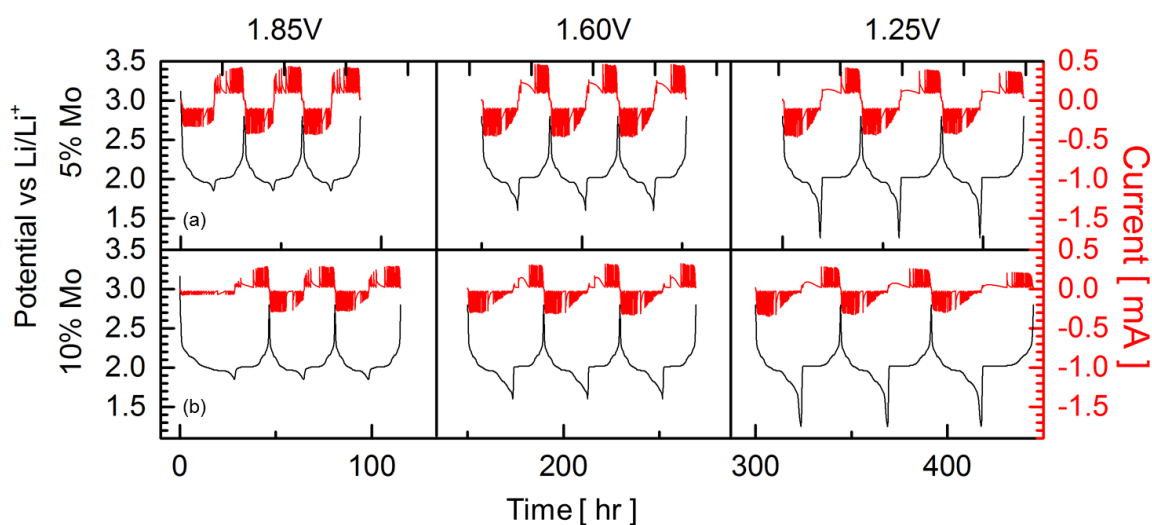


Figure 3-10 PITT results for 5% Mo (a) and 10% Mo (b) to different cutoff voltages with a 10mV step and 2mA \cdot g⁻¹ current cutoff.

3.2.2 Phase Evolution

To understand the changes in the lithiation reaction preceding the multiphase reaction region, several *ex-situ* X-ray diffraction studies were completed. Cells were discharged to similar voltage cutoffs and Li_x values to compare the discharge mechanisms.

For the 1.90V cutoff, the *ex-situ* XRD in Table 3-5 data reveal similar lattice volumes circa 773 \AA^3 for all samples. In contrast, the lower 1.75V discharge reveals a distinct and systematic increase in lattice volume as a function of Ta substitution. The unsubstituted sample shows a slight increase in volume to 778 \AA^3 whereas the substituted samples of 5% and 10% Ta show a significant increase in volume to 795 \AA^3 and 797 \AA^3 , respectively. The volume expansion to 788 \AA^3 for the highly 20% substituted sample reverts the trend slightly while still showing a significantly greater volume than the unsubstituted sample. The increase in volume for the lithiated Ta substituted samples is manifested as a systematic increase in the b and c lattice parameters while maintaining relatively invariant a lattice parameter and β angle. This may be due to the decreased values of Li insertion observed for this sample.

Looking specifically at the unsubstituted samples and the 10% Ta sample presents an ideal comparison with similarly intercalated Li_x values of 0.694 and 0.667 at 1.90V and 0.814 and 0.827 at 1.75V respectively. In addition, these two samples demonstrate a distinct contrast in electrochemical stability and phase progression upon delithiation via PITT. At 1.90V, the unsubstituted lattice volume of 773.2 \AA^3 is in close agreement with the 10% Ta substitution lattice volume of 775.3 \AA^3 . At the lower voltage of 1.75V, a significant contrast in lattice volume of 775.3 \AA^3 for the unsubstituted $\beta\text{-NbPO}_5$ exists

with that of 797.1 Å³ for the 10% Ta. To recall, this lower voltage region where the lattice volume difference is observed also contains the electrochemically deleterious region for the unsubstituted sample as demonstrated by the change in discharge cutoff potential (Fig. 3-5a). The Rietveld fit and difference plots for the 1.75V and 1.90V samples of the unsubstituted and 10% Ta substituted samples are shown for examination in Fig. 11 and no sign of second phases is apparent. The 5% and 10% Mo substituted samples also show little expansion in volume at 1.75V similar to the unsubstituted sample and consistent with the electrochemical characteristics they share. As seen before in the PITT experiments, the 2% Ta, 5% Mo and 10% Mo act similarly to the unsubstituted sample with little to no shifts in the main peaks.

Table 3-5 Rietveld analysis of patterns *ex-situ* cells.

Sample	x value	wt%	GOF	a [Å]	b [Å]	c [Å]	Beta [°]	Volume [Å ³]
0% Ta 1.90V	0.694	100	2.83	13.22(7)	5.15(2)	13.08(8)	119.92(5)	773.21(1)
0% Ta 1.75V	0.814	100	2.30	13.17(3)	5.13(7)	13.24(8)	119.75(5)	778.41(6)
2% Ta 1.90V	0.732	100	2.03	13.22(1)	5.16(0)	13.07(9)	119.98(0)	773.02(1)
2% Ta 1.75V	0.858	100	2.19	13.22(7)	5.10(6)	13.31(4)	120.14(7)	777.79(0)
5% Ta 1.90V	0.780	100	1.66	13.22(4)	5.15(4)	13.08(2)	119.93(1)	772.87(2)
5% Ta 1.75V	0.901	100	2.92	13.11(6)	5.21(9)	13.39(6)	119.86(8)	795.32(3)
10% Ta 1.90V	0.667	93.4	1.88	13.18(1)	5.14(8)	13.13(6)	119.58(7)	775.29(6)
10% Ta 1.75V	0.827	95.1	2.07	13.10(1)	5.23(6)	13.88(1)	119.74(5)	797.12(6)
20%Ta 1.90V	0.592	91.7	2.33	13.15(0)	5.19(1)	13.06(0)	119.87(7)	773.14(5)
20%Ta 1.75V	0.789	99.0	2.00	13.15(3)	5.16(0)	13.37(8)	120.02(4)	786.25(8)
5% Mo 1.90V	0.611	100	2.16	13.20(8)	5.13(9)	13.09(0)	120.02(6)	769.39(8)
5% Mo 1.75V	0.775	100	2.09	13.13(9)	5.20(4)	13.01(6)	119.91(3)	771.54(4)
10% Mo 1.90V	0.797	100	2.00	13.23(1)	5.15(2)	13.09(5)	119.94(7)	773.67(7)
10% Mo 1.75V	0.888	100	1.76	13.25(6)	5.13(8)	13.14(7)	120.02(1)	775.35(0)

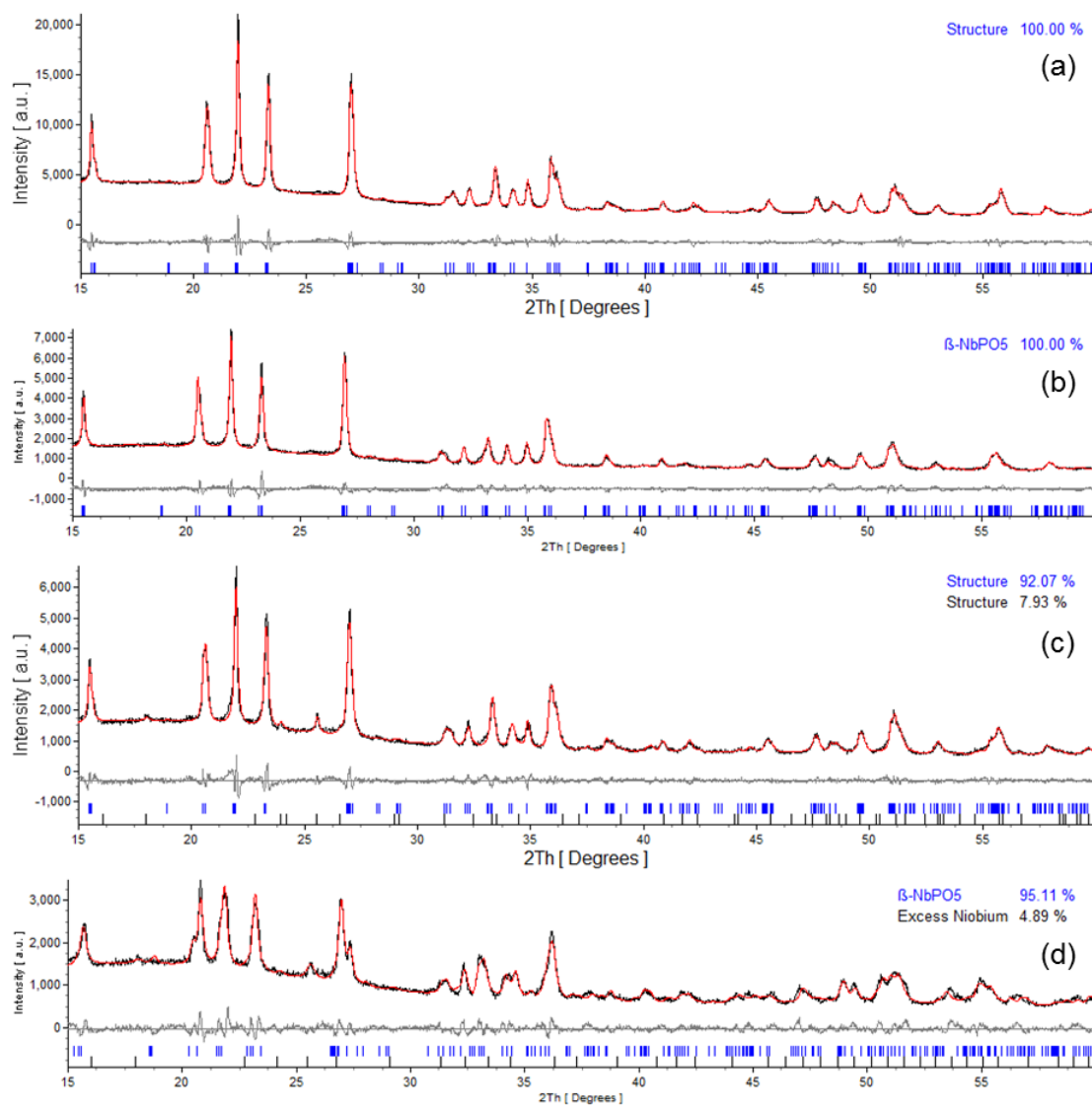


Figure 3-11 Rietveld analysis of 0% Ta at 1.90V (a) and 1.75V (b) and 10% Ta at 1.90V (c) and 1.75V (d). Black lines are experimental data, red lines are theoretical, and gray lines are difference calculations.

Additional *ex-situ* XRD experiments in Fig. 3-12 and Fig. 3-13 further demonstrate the disparity between the discharge/charge mechanisms in the unsubstituted and 10% Ta samples of contrasting electrochemical performance. The XRD patterns are shown for the delithiation area where the PITT of the unsubstituted samples suggests a strong two phase behavior and the 10% substituted has none. Examination of the unsubstituted reflections (Fig. 12) during delithiation reveal a systematic increase in a second monoclinic phase reflection. Although occurring throughout the XRD pattern, these are most clearly seen by the development of the peaks at approximately 16° , 21° , 27° , and 31° 2θ , while the other Bragg reflections remain invariant. The initial and new monoclinic phase that has developed is listed in Table 3-6 ($x = 0.82$ (a) vs. $x = 0.3$ (e)).

The similar region of Li_x shown in the XRD patterns of delithiation shown for 10% substitution in Fig. 13 reveals a sharply contrasting behavior. As discussed earlier, the Ta substituted material has a significantly larger unit cell upon lithiation. The process of delithiation in the flatter, but sloped region of $x = 0.75$ to $x = 0.35$ (a-e), reveal that the monoclinic structure goes through a systematic shrinkage of the unit cell. This is represented by a continuous change in Bragg reflection position and thus lattice parameter. Systematic shifts are visually apparent in the Bragg reflections at approximately 21° , 27° , and 31° although most peaks do show systematic changes in peak position. Table 3-7 shows that the refined lattice parameters in this region systematically decrease for b and c while a and β remain relatively invariant. This is the reverse of the trend in lattice parameter development we have shown for the Ta substituted versus non Ta substituted during lithiation.

In summary, much improved cycling for β -NbPO₅ is manifested when the lower lithiation voltage is raised suggesting a failure mode associated with a phase transition induced by higher degrees of lithiation approaching $x = 1$. Lower voltage cycling is shown to be much improved by 5 to 20% Ta substitution within β -NbPO₅. This improved cycling seems to be associated with a distinct change in phase development. Although unsubstituted and substituted β -NbPO₅ initially have similar lattice parameters, upon lithiation the Ta substituted β -NbPO₅ has a significantly larger monoclinic unit cell. Upon delithiation, the slope of the voltage profile, high resolution PITT, and *ex-situ* XRD reveals that the delithiation reaction progresses as a two phase monoclinic reaction for the unsubstituted β -NbPO₅ while Ta substituted β -NbPO₅ evolves as single phase reaction. While the voltage is not necessarily optimal for a high energy battery, Ta substituted β -NbPO₅ represents a model of lithium insertion phosphates with near 0% irreversible loss, excellent cycling stability, and excellent 20C rates in large grains without the formation of a nanocomposite.

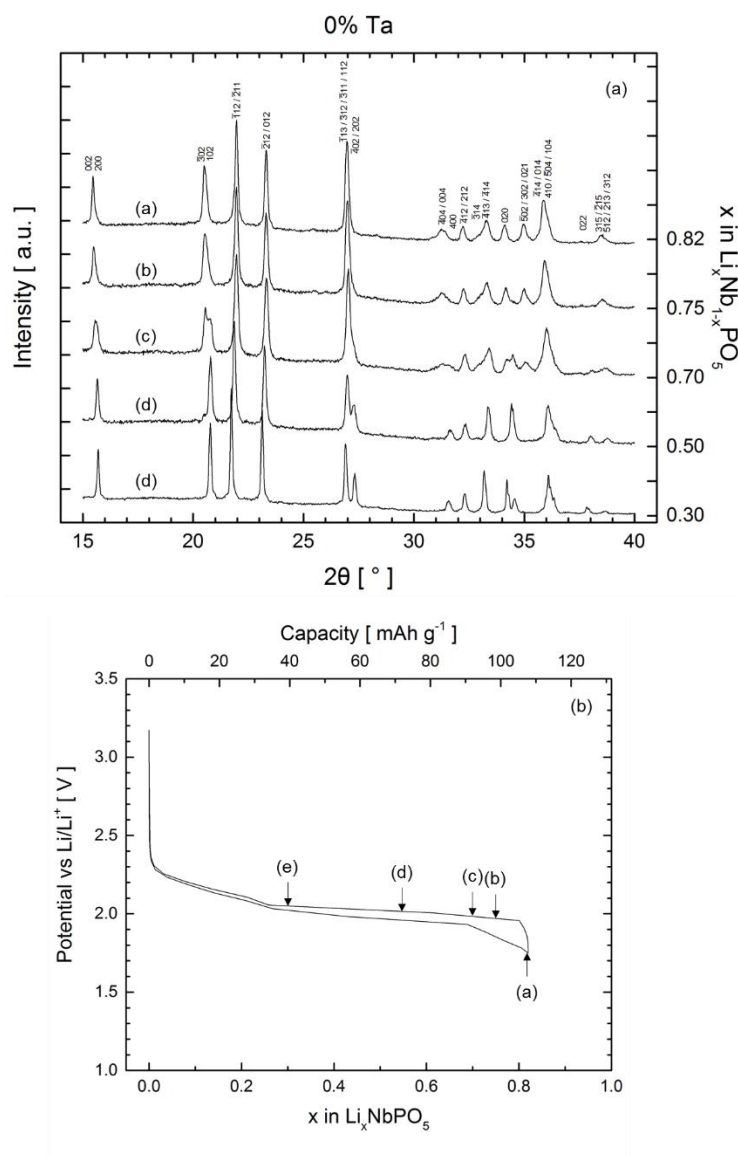


Figure 3-12 *Ex-situ* XRD patterns of unsubstituted samples during delithiation (a) corresponding with their respective positions in the voltage profile (b).

Table 3-6 Rietveld analysis of *ex-situ* XRD of the unsubstituted samples.

x in $\text{Li}_x\text{Nb}_{1-x}\text{PO}_5$	GOF	a [Å]	b [Å]	c [Å]	Beta [°]	Volume [Å ³]
0.82	2.16	13.26(1)	5.13(4)	13.16(0)	120.01(6)	776.01(7)
0.75	2.04	13.19(6)	5.13(7)	13.17(4)	119.66(8)	776.08(0)
0.70	2.62	13.22(1)	5.15(0)	13.15(4)	120.40(6)	772.62(2)
0.55	1.64	13.12(1)	13.05(5)	13.05(5)	120.01(8)	773.84(3)
0.30	1.76	13.08(8)	13.12(5)	13.12(5)	120.22(5)	778.25(7)

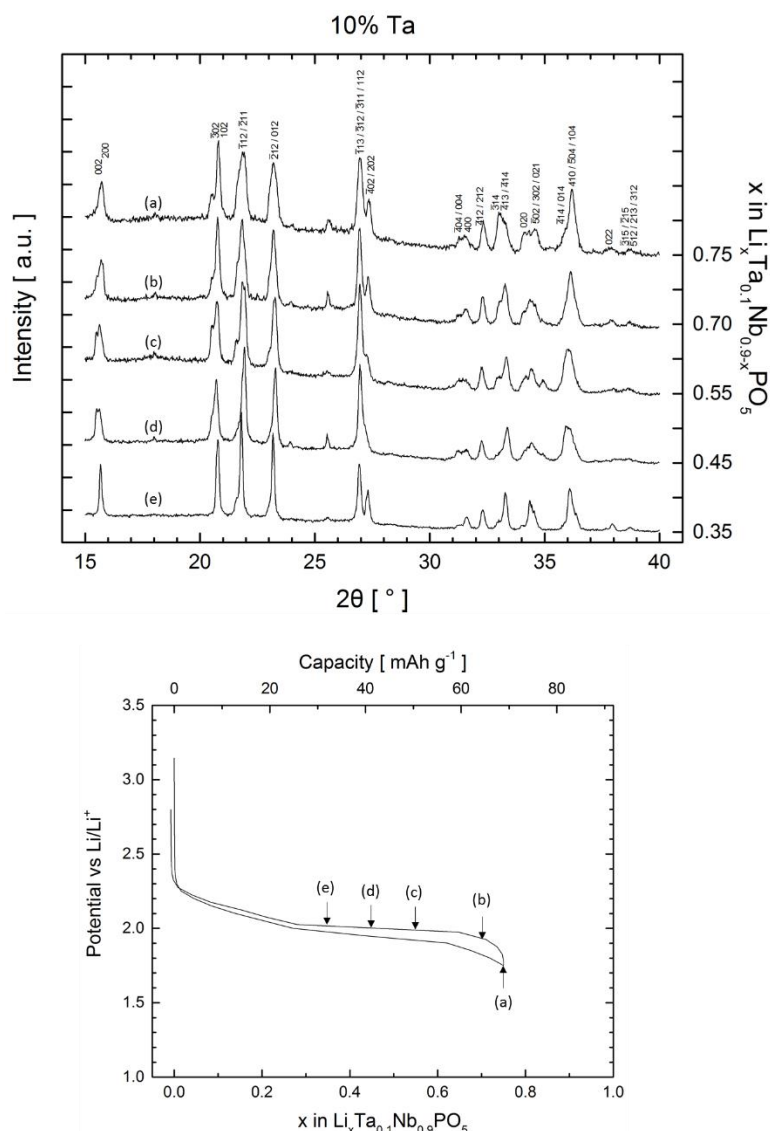


Figure 3-13 *Ex-situ* XRD patterns of 10% Ta samples during delithiation (a) corresponding with their respective positions in the voltage profile (b).

Table 3-7 Rietveld analysis of *ex-situ* XRD of 10% Ta samples.

$\text{Li}_x\text{Ta}_{0.1}\text{Nb}_{0.9-x}\text{PO}_5$	GOF	a [Å]	b [Å]	c [Å]	Beta [°]	Volume [Å ³]
0.75	2.38	13.10(1)	5.25(6)	13.23(2)	120.09(2)	788.39(7)
0.70	2.47	13.10(5)	5.23(4)	13.14(2)	120.14(1)	779.66(8)
0.55	2.66	13.20(7)	5.19(7)	13.10(1)	120.07(7)	778.22(1)
0.45	2.32	13.20(0)	5.18(7)	13.08(7)	119.98(1)	776.27(7)
0.35	2.00	13.10(1)	5.20(2)	13.01(4)	120.00(4)	768.25(8)

4 Future Work

Rietveld analysis will be continued on the *ex-situ* XRD patterns to identify the phases present during lithiation and delithiation of the unsubstituted and 10% Ta substituted phases.

The study of $\beta\text{-Ta}_x\text{Nb}_{1-x}\text{PO}_5$ raises additional questions and theories for testing that are outside of the scope and/or timeframe of this thesis. Further studies may reveal other enhancements or further detail the reaction mechanisms.

Additional insights on the $\beta\text{-Ta}_x\text{Nb}_{1-x}\text{PO}_5$ system and the reaction mechanisms can be realized through Scanning Electron Microscopy (SEM). The irreversible drop in capacity after the high rate cycling protocol can be analyzed to see if any fracturing or structural changes occur after cycling at high rates. Prolonged cycling induces stresses and a study on the physical changes over time could shed light on techniques to improve cycling stability.

Energy Dispersive Spectroscopy (EDS) characterization can reveal the distribution of phosphorus and confirm if there is an effect resulting from the degree of mixedness. Additionally, the distribution of Ta can be studied to monitor any physical or electrochemical changes. Other ionic substitutions outside of Ta, Mo, W, V, Co, and Ga can be tested to see if a similar effect can be produced. SEM and EDS may also provide insight on how to improve the purity of $\beta\text{-Ta}_x\text{Nb}_{1-x}\text{PO}_5$ when $x \geq 10$.

Galvanostatic Intermittent Titration Technique (GITT) is an additional high resolution electrochemical characterization technique that can be utilized to identify the true equilibrium potential of the two-phase reaction and to determine if near theoretical specific capacities can be achieved.

The tetragonal α -NbPO₅ and orthorhombic Nb_{1.91}P_{2.82}O₁₂ are also open for investigation. Patoux previously studied the electrochemistry of the tetragonal phase, but no modifications have improved the electrochemical stability. The orthorhombic phase remains unstudied. Synthesis methods for higher purities of the orthorhombic phase are needed (>95%) for more accurate electrochemical characterization. Similar methods used to purify and test the monoclinic β -NbPO₅ can be employed for the tetragonal and orthorhombic phases to see if any benefits exist.

5 Summary

The improvement on the electrochemical stability of β -NbPO₅ is realized through two approaches. Altering the voltage window to avoid the <1.8V region allows the lower voltage reaction to be avoided while simultaneously improving the cycling stability. The addition of Ta to form β -Ta_xNb_{1-x}PO₅ with $x \geq 5$ also produces a similar effect on avoiding the lower voltage reaction while allowing a greater voltage window down to 1.75V. Through the use of a comprehensive series of PITT and XRD analyses, this improvement was correlated to a distinct change in the two phase delithiation pathway for the β -NbPO₅ versus that of the two phase reaction for β -Ta_xNb_{1-x}PO₅. The cycling of the end member β -TaPO₅ confirms the effect of substitution while also reporting the electrochemistry for the first time. β -NbPO₅ retains 93% of its initial capacity (98 mAh·g⁻¹) after 100 cycles at a C/15 rate with a voltage window of 2.8V to 1.85V. β -Ta_{0.1}Nb_{0.9}PO₅ retains 93% capacity (85 mAh·g⁻¹) after 100 cycles at a C/4 rate with a voltage window of 2.8V to 1.75V. Both materials demonstrate exceptional reversibility along with extremely low polarization at an operating voltage circa 2V, making this material a good candidate for a model reference electrode material.

6 References

1. Kurzweil, P. Gaston Planté and His Invention of the Lead-Acid Battery-The Genesis of the First Practical Rechargeable Battery. *J. Power Sources* **195**, 4424–4434 (2010).
2. Nagaura, T; Tozawa, K. Lithium-Ion Rechargeable Battery. *Prog. Batter. Sol. Cells* **9**, 209–215 (1990).
3. Wang, F., Robert, R., Chernova, N. a, Pereira, N., Omenya, F., Badway, F., Hua, X., Ruotolo, M., Zhang, R., Wu, L., Volkov, V., Su, D., Whittingham, M. S., Grey, C. P., Amatucci, G. G., Zhu, Y., Graetz, J., Omenya, F. & Bad-, F. Conversion Reaction Mechanisms in Lithium Ion Batteries: Study of the Binary Metal Fluoride Electrodes Conversion Reaction Mechanisms in Lithium Ion Batteries: Study of the Binary Metal Fluoride Electrodes. 1–10 (2011). doi:10.1021/ja206268a
4. Cabana, J., Monconduit, L., Larcher, D. & Palacín, M. R. Beyond Intercalation-Based Li-ion Batteries: The State of the Art and Challenges of Electrode Materials Reacting Through Conversion Reactions. *Adv. Mater.* **22**, 170–192 (2010).
5. Tarascon, J.-M. Is Lithium the New Gold? *Nat. Chem.* **2**, 510 (2010).
6. Wang, Q., Ping, P., Zhao, X., Chu, G., Sun, J. & Chen, C. Thermal Runaway Caused Fire and Explosion of Lithium Ion Battery. *J. Power Sources* **208**, 210–224 (2012).
7. Tarascon, J. M. & Armand, M. Issues and Challenges Facing Rechargeable Lithium Batteries. *Nature* **414**, 359–367 (2001).
8. Boukamp, B.A.; Lesh, G.C.; Huggins, R. A. All-Solid Lithium Electrodes with Mixed-Conductor Matrix. 725–729 (1981).
9. Besenhard, J. O. & Winter, M. Advances In Battery Technology: Rechargeable Magnesium Batteries and Novel Negative-Electrode Materials for Lithium Ion Batteries. *ChemPhysChem* **3**, 155–159 (2002).
10. Ohzuku, T. Zero-Strain Insertion Material of $\text{Li}[\text{Li}_{1/3}\text{Ti}_{5/3}]\text{O}_4$ for Rechargeable Lithium Cells. *J. Electrochem. Soc.* **142**, 1431 (1995).
11. Lewandowski, A. & Świdarska-Mocek, A. Ionic Liquids as Electrolytes for Li-Ion Batteries-An Overview of Electrochemical Studiess. *J. Power Sources* **194**, 601–609 (2009).

12. Padhi, A.K.; Nanjundaswamy, K.S.; Goodenough, J. B. Phospho-olivines as Positive-Electrode Materials for Rechargeable Lithium Batteries. *J. Electrochem. Soc.* **144**, 1188–1194 (1997).
13. Hahn, R. B. Phosphates of Niobium and Tantalum. *J. Am. Chem. Soc.* **73**, 5091–5093 (1951).
14. Levin, E. M. & Roth, R. S. The System Niobium Pentoxide-Phosphorus Pentoxide. *J. Solid State Chem.* **2**, 250–261 (1970).
15. Chahboun, H. & Raveau, B. β -NbPO₅ and β -TaPO₅: Bronzoids, Second Members of the Monophosphate Tungsten Bronze Series (PO₂)₄(WO₃)_{2m}. **342**, 331–342 (1986).
16. Leclaire, A.; Chahboun, H.; Groult, D.; Raveau, B. The Crystal Structure of β -NbPO₅. *Zeitschrift für Krist.* **177**, 277–286 (1986).
17. Wang, X., Huang, Q., Deng, J., Yu, R., Chen, J. & Xing, X. Phase Transformation and Negative Thermal Expansion in TaVO₅. *Inorg. Chem.* **50**, 2685–2690 (2011).
18. Patoux, S. & Masquelier, C. Lithium Insertion Into Titanium Phosphates, Silicates, and Sulfates. *Chem. Mater.* **14**, 5057–5068 (2002).
19. Gatehouse, B. M., Platts, S. N. & Williams, T. B. Structure of Anhydrous Titanyl Sulfate, Titanyl Sulfate Monohydrate and Prediction of a New Structure. *Acta Crystallogr. Sect. B Struct. Sci.* **49**, 428–435 (1993).
20. Gnanavel, M., Raveau, B. & Pralong, V. Electrochemical Li/Na Intercalation in TiOSO₄, First Member of the Phosphate Tungsten Bronze-Type Family. *J. Electrochem. Soc.* **162**, A465–A469 (2015).
21. Lim, S.; Vaughey, J.T.; Harrison, W.T.A.; Dussack, L.L.; Jacobson, A.J.; Johnson, J. W. Redox Transformations of Simple Vanadium Phosphates: the Synthesis of ϵ -VOPO₄. *Solid State Ionics* **84**, 219–226 (1996).
22. Kerr, T. A. Highly Reversible Li Insertion at 4 V in ϵ -VOPO₄/ α -LiVOPO₄ Cathodes. *Electrochem. Solid-State Lett.* **3**, 460 (2000).
23. Wang, S. L., Wang, C. C. & Lii, K. H. Crystal Structure of WPO₅, the Second Member of the Monophosphate Tungsten Bronze Series (WO₃)_{2m}(PO₂)₄. *J. Solid State Chem.* **82**, 298–302 (1989).
24. Baran, E. J., Botto, I. L., Kinomura, N., Kumada, N. & Baran, E.J.; Botto, I.L.; Kumada, N. The Infrared Spectra of the Two Polymorphic Forms of WOPO₄. *J. Solid State Chem.* **89**, 144–146 (1990).

25. Patoux, S. & Masquelier, C. Chemical and Electrochemical Insertion of Lithium Into Two Allotropic Varieties of NbPO₅. *Chem. Mater.* **14**, 2334–2341 (2002).
26. Chernorukov, N.G.; Egorov, N.P.; Mochalova, I. R. Zh. Neorg. Khim. *Russ. J. Inorg. Chem (Engl. Transl.)* **23**, 1627–1629 (1978).
27. Imanishi, N.; Matsuoka, K.; Takeda, Y.; Yamamoto, O. ABO₄ Type Electrode Materials for Rechargeable Lithium Battery. *Denki Kagaku* **61**, 1023–1024 (1993).
28. H. Eick, L. K. The Crystal Structure of VOMoO₄. *Acta Chem. Scand.* **20**, 722–729 (1966).
29. Shannon, R. D. Revised Effective Ionic Radii and Systematic Studies of Interatomic Distances in Halides and Chalcogenides. *Acta Crystallogr. Sect. A* **32**, 751–767 (1976).
30. Amarilla, J.M. ; Casal, B.; Galvan, J.C.; Ruiz-Hitzky, E. Lithium-MVO₅ (M = Nb, Ta) Bronzes. *Chem. Mater.* 62–67 (1992).
31. Zhu, J. & Huang, Y. Solid-State NMR Study of Dehydration of Layered α -Niobium Phosphate. *Inorg. Chem.* **48**, 10186–10192 (2009).
32. Mukherjee, G. D., Vijaykumar, V., Karandikar, a. S., Godwal, B. K., Achary, S. N., Tyagi, a. K., Lausi, A. & Busetto, E. Compressibility Anomaly and Amorphization in the Anisotropic Negative Thermal Expansion Material NbOPO₄ Under Pressure. *J. Solid State Chem.* **178**, 8–14 (2005).
33. Gozdz, A. S. . & Schmutz, C; Tarascon, J.M.; Warren, P. Polymeric Electrolytic Cell Separator Membrane. *US Patent 5,418,091* (1995). at <<http://www.google.com/patents?hl=en&lr=&vid=USPAT5418091&id=vd0ZAAAEBAJ&oi=fnd&dq=Polymeric+Elecrolyte+Cell+Separator+Membrane&prints=abstract>>
34. Wen, C. B. & BA; Huggins, R. Thermodynamic and Mass Transport Properties of ‘LiAl’. *Electrochem. Soc.* **126**, 2258–2266 (1979).
35. Han, B. C., Van Der Ven, A., Morgan, D. & Ceder, G. Electrochemical Modeling of Intercalation Processes with Phase Field Models. *Electrochim. Acta* **49**, 4691–4699 (2004).
36. Haider, S. Z. Niobium and Tantalum Phosphates. *Proc. Pak. Acad. Sci* **1**, 19–28 (1964).
37. LeClaire, A.; Chahboun, H.; Groult, D.; Raveau, B. The Crystal Structure of β -NbPO₅. *Zeitschrift für Krist.* **177**, 277–286 (1986).